Environmental Pollution 397 (2026) 128030

Contents lists available at ScienceDirect

Environmental Pollution

journal homepage: www.elsevier.com/locate/envpol

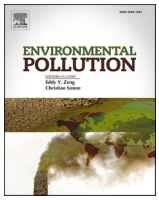

Fibrous zeolites and pulmonary fibroblasts: toxicological impact and EPR-based insights into cellular alterations

Matteo Giordani [a], Maria Gemma Nasoni [b], Erik Bargagni [b], Michela Cangiotti [a], Francesca Luchetti [b], Michele Mattioli [a,*]

[a] Department of Pure and Applied Sciences, University of Urbino Carlo Bo, 61029, Urbino, Italy
[b] Department of Biomolecular Sciences, University of Urbino Carlo Bo, 61029, Urbino, Italy

ARTICLE INFO

Keywords:
Zeolite fibers
MRC-5 fibroblasts
EPR spectroscopy
CAT16 probe
Cytotoxicity

ABSTRACT

This study investigates the potential cytotoxicity of the carcinogenic erionite and other fibrous zeolites, including mordenite, ferrierite and scolecite. Their interactions with human lung fibroblast cells (MRC-5) were evaluated using biological assays combined with Electron Paramagnetic Resonance (EPR) spectroscopy. All fibrous zeolites were found to interact with lung fibroblasts, leading to increased intracellular ROS levels and alterations in the lysosomal compartment after 24 h of exposure. EPR measurements after CAT16 incubation provided further insight into cellular membrane interaction dynamics, revealing notable differences in spectral intensity and hyperfine coupling constants, which suggest distinct interaction mechanisms among the fibers. Erionite showed the highest radical solubilization, implying potential cytotoxic effects. Prolonged exposure to mordenite and ferrierite also significantly reduced cell viability, at levels comparable to erionite. These findings highlight key factors involved in early inflammatory responses and their potential contribution to the development of long-term chronic diseases and cancer. The biological effects of fibrous zeolites are controlled by a multifactorial interplay between morphology, surface area, chemical composition, and biopersistence, which together determine the extent of membrane interaction, oxidative stress generation, and intracellular processing, ultimately governing cytotoxicity and potential carcinogenicity. This study therefore provides an initial step toward understanding the biological mechanisms underlying the toxicity and carcinogenic potential of fibrous zeolites, improving awareness of their potential human health risks.

1. Introduction

Fibrous minerals have been a health concern since the link between asbestos minerals and lung disease was clearly established several decades ago. Since then, researchers from fields such as mineralogy and medicine have extensively investigated this issue. In general, elongated particles are considered "inhalable" by humans if their diameter is below 3.5 μm (Lee, 1985). For regulatory purposes, the fibers of greatest concern have a diameter-to-length ratio of ≤1:3, a diameter <3 μm, and a length >5 μm (WHO, 1986; NIOSH, 1994a; 1994b). Most information on the carcinogenicity and toxicity of fibrous minerals comes from studies on asbestos minerals and fibrous erionite. However, the health effects of many other inhalable mineral fibers remain poorly understood. Due to their established carcinogenicity, asbestos minerals (chrysotile, amosite, crocidolite, asbestos anthophyllite, asbestos tremolite, and asbestos actinolite) and fibrous erionite are classified as Group 1 carcinogens by the International Agency for Research on Cancer (IARC, 2012).

Erionite has been identified as a human carcinogen based on extensive research in epidemiology, medicine, biology, mineralogy, and related fields. Concerns about its health risks from environmental and occupational exposure have been reported in several countries, including Turkey, the United States, Mexico, Iran, Italy, and New Zealand (Carbone et al., 2011; Saini-Eidukat and Triplett, 2014; Ortega--Guerrero and Carrasco-Núñez, 2014; Ilgren et al., 2015; Giordani et al., 2017; Patel and Brook, 2021). Based on these findings, the IARC (1997) emphasized the need for further research on other fibrous minerals, particularly those with characteristics similar to erionite and asbestos.

Zeolites, including erionite, have attracted growing attention because of their widespread environmental occurrence and broad industrial applications (Armbruster and Gunter, 2001; Ming and Allen, 2001; Eroglu et al., 2017). These minerals exhibit properties such as

* Corresponding author.
E-mail address: michele.mattioli@uniurb.it (M. Mattioli).

https://doi.org/10.1016/j.envpol.2026.128030
Received 24 January 2026; Received in revised form 12 March 2026; Accepted 26 March 2026
Available online 27 March 2026

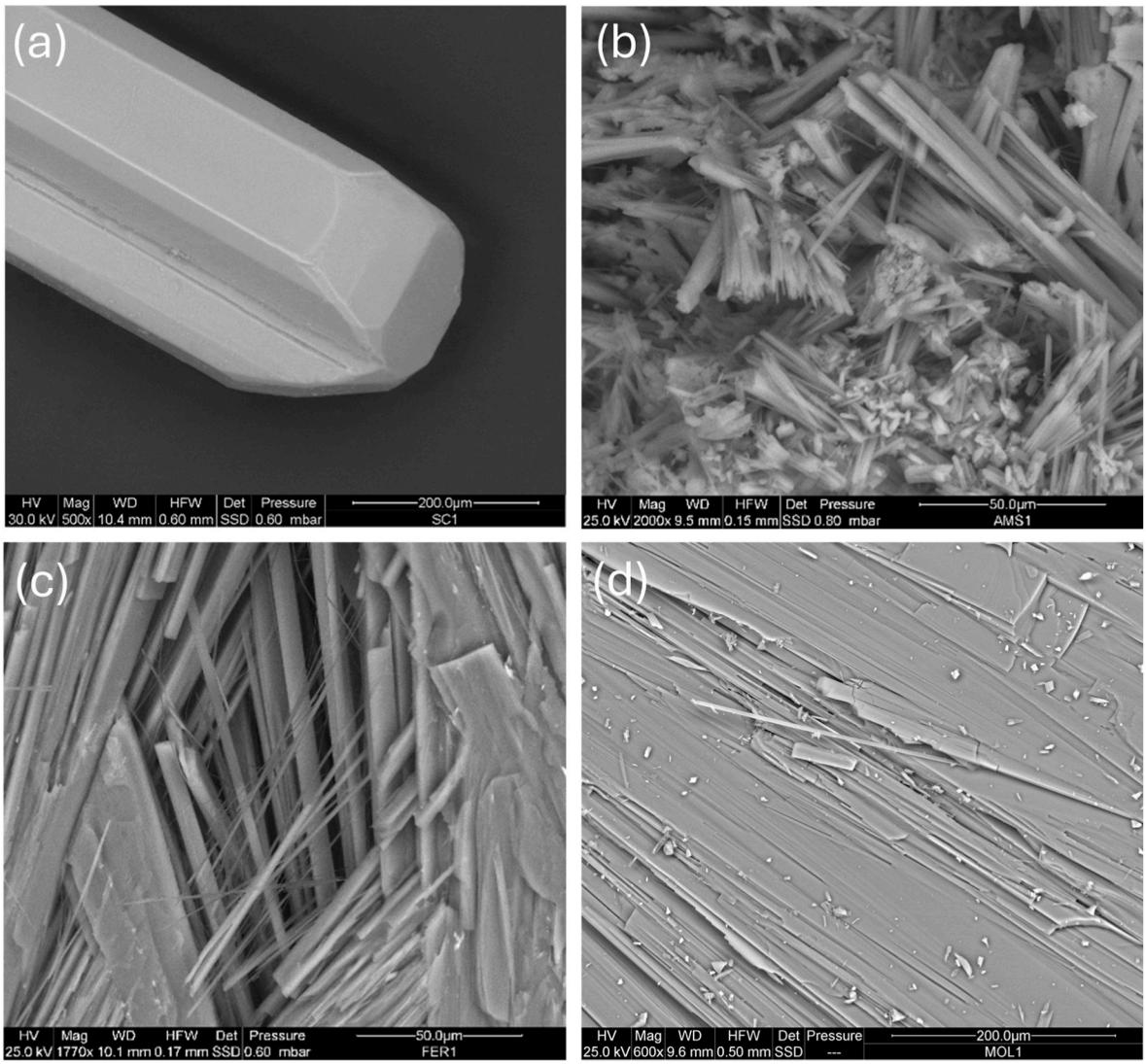

Fig. 1. SEM images of the investigated zeolite fibers: (a) prismatic, elongated crystal of scolecite (SC1); (b) erionite with an extremely fibrous, needle-like habit (AMS1); (c) acicular to fibrous ferrierite crystals (FER5); (d) fibrous mordenite crystals grouped in roughly prismatic forms (MOL1).

cation exchange, molecular sieving, adsorption, and catalysis. However, only a few zeolite species have been evaluated for potential health risks. Given the limited evidence, the IARC currently classifies fibrous clinoptilolite, phillipsite, and mordenite fibers as Group 3 carcinogens (IARC, 1997), meaning their carcinogenicity is not confirmed. Identifying zeolites that may pose health risks is therefore essential. Recent studies have examined the physicochemical properties of zeolites such as erionite (Ballirano et al., 2018; Beaucham et al., 2018; Giordani et al., 2017), mordenite (Di Giuseppe, 2020; Giordani et al., 2022a), offretite (Giordani et al., 2019; Mattioli et al., 2018), ferrierite (Gualtieri et al., 2018a,b; Zoboli et al., 2019; Mattioli et al., 2022), scolecite (Mattioli et al., 2016), mesolite, and thomsonite (Giordani et al., 2022b; Betti et al., 2022), though many aspects of their biological impact remain unknown.

Mordenite, one of the most widely used zeolites in both natural and synthetic forms, plays a key role in industrial applications, including petrochemical processing, catalysis, semiconductors, chemical sensors, methylamine synthesis, and gas-liquid separation (Corma et al., 1994; Niwa et al., 2010; Zhou and Boyd, 2014; Wahono et al., 2020; Narayanan et al., 2021). Despite its physicochemical similarities to the carcinogenic erionite, mordenite is currently classified as a Group 3 carcinogen by the IARC. To date, only a limited number of in vitro and in vivo studies have investigated its health effects (Suzuki, 1982; Suzuki and Kohyama, 1984, 1988; Tátrai et al., 1992; Adamis et al., 2000; Palekar et al., 1988; Fach et al., 2003), making further research particularly relevant. Several earlier studies were methodologically limited, using non-fibrous or impure samples, unspecified fiber proportions, short exposure durations, small sample sizes, or lacking survival data (Guthrie, 1992; IARC, 1997). More recent studies have investigated the potential inhalation hazards of mordenite (Stephenson et al., 1990; Di Giuseppe, 2020; Giordani et al., 2022a) and ferrierite (Gualtieri et al., 2018a,b; Mattioli et al., 2022). Mordenite is generally considered less hazardous than erionite and shows different cytotoxic behavior, with no evidence of mutagenicity (Fach et al., 2003). In contrast, the toxicological profile of ferrierite remains comparatively underexplored.

This study aims to characterize four natural fibrous zeolites (scolecite, carcinogenic erionite, ferrierite and mordenite) from morphological, mineralogical, chemical, interacting ability, and in-vitro toxicity perspectives, to improve understanding of these fibers and provide preliminary insights into potential health risks. First, morphological and morphometric analyses were carried out using environmental scanning electron microscopy with energy-dispersive spectroscopy (ESEM-EDS), X-ray fluorescence (EDXRF) and X-ray powder diffraction (XRPD), alongside mineralogical and chemical characterizations. These aspects are crucial for understanding inhalation behavior, deposition patterns in the lungs, fiber-lung tissue interactions, and the release or exchange of

elements and contaminants (e.g., Stanton et al., 1981; Aust et al., 2001; Boulanger et al., 2014; Heyder et al., 1986; Giordani et al., 2022c; Bloise et al., 2020; Salucci et al., 2024; Gualtieri, 2023). Second, electron paramagnetic resonance (EPR) spectroscopy was used to assess the interaction abilities of these zeolites with human cells in the presence of the radical probe CAT16, offering insights into their surface and structural properties (Mattioli et al., 2016, 2022; Cangiotti et al., 2017, 2018; Giordani et al., 2022b; Gualtieri et al., 2018a,b; Pugnaloni et al., 2023). Finally, their toxicity was assessed through in vitro experiments using the human primary pulmonary fibroblast cell line (MRC-5) to evaluate biological effects and potential health risks (Stan et al., 2021). Cell viability and toxicity were assessed via Trypan Blue assay and calcein staining. Additionally, intracellular oxidative stress and lysosomal alterations were also analyzed, as these factors are key drivers of early inflammatory response and potential contributors to chronic diseases and malignancies over time.

2. Materials and methods

2.1. Materials

This study examined four fibrous zeolite samples (Fig. 1): scolecite (SC1), erionite (AMS1, proven human carcinogen), and two potentially toxic species, ferrierite (FER5) and mordenite (MOL1).

The scolecite sample (SC1) originates from Nasik, Pune District, India. It forms prismatic, elongated crystals with diameters ranging from 0.5 to 3 mm, typically arranged in irregular or radiating clusters. Unlike other fibrous zeolites, scolecite shows little to no tendency to form thin fibers. As it is considered a non-carcinogenic fibrous mineral, it was included as a comparative reference.

The erionite sample (AMS1) was collected from the Ash Meadows Zeolite deposits in Shoshone, Dublin Hills, Inyo County, California, USA. These deposits mainly consist of mudstone and rhyolitic volcanic ash layers. Erionite occurs either as monomineralic layers or in association with clinoptilolite, chabazite, phillipsite, clay, potassium feldspar, and occasionally opal. In contrast to the woolly-looking erionite from the type locality in Durkee, Oregon (Eakle, 1898), the Ash Meadows specimen exhibits a distinctly fibrous, needle-like morphology, forming random networks of crystals that often display radiating clusters.

The ferrierite sample (FER5) originates from Albero Bassi in Santorso, Vicenza Province, Veneto, Italy. It occurs as a secondary mineral within voids and cavities of fine-grained basalt flows from the Tertiary Veneto Volcanic Province in Northern Italy. The most common habit consists of orange-reddish, transparent, thin blades, accompanied by needle-like or fibrous crystals less than 1 mm in size that fill the cavities. In approximately 15% of the cavities, ferrierite forms spherical to subspherical aggregates (up to 2 mm) composed of densely packed, colorless, needle-like, or fibrous crystals, partially or completely lining the cavity walls.

The mordenite sample (MOL1) was collected from the Monte Oladri quarry in Monastir, Southern Sardinia, Italy. It occurs as a secondary phase within cavities of a weathered, highly zeolitized basaltic-andesitic sequence of the Cenozoic age. These rocks have a crystalline groundmass rich in glass and plagioclase microphenocrysts. The dominant zeolites are analcime and heulandite, with lesser amounts of mesolite, mordenite, and chabazite. Mordenite typically forms thin, fibrous crystals, often grouped into roughly prismatic aggregates. It is commonly associated with ferrierite in orange spherical clusters of radiating blades, reaching up to 15 mm in diameter.

Several pure fibrous crystals were manually extracted from the matrix of each sample using a stereoscopic optical microscope. Fiber fractions were selected according to the specific requirements of each experimental method.

2.2. Environmental scanning electron microscopy (ESEM)

Morphological observations were conducted using an Environmental Scanning Electron Microscope (ESEM) FEI Quanta 200 FEG, equipped with an energy-dispersive X-ray spectrometer (EDS) for microchemical analysis. The settings included a 25 kV accelerating voltage, adjustable beam diameter, a working distance of 10-12 mm, and a tilt angle of 0°. The ESEM operated in low vacuum mode, with the chamber pressure between 0.80 and 0.90 mbar. Images were captured using a single-shot detector (SSD) or an Everhart–Thornley secondary electron detector (ETD), and measurements of fibers widths and lengths were taken from over 1000 fibrils in these images. Qualitative chemical data were also collected from various points on selected crystals to assess compositional uniformity, and additional analyses targeted impurities on the crystal surface.

The microchemical analysis of MOL1 was performed with a Zeiss Gemini SEM 450 Scanning Electron Microscope coupled with an EDX detector (Oxford Instruments X-Max 150), operating at a 10 kV voltage and 200 pA current. Low counting time (10 s) to minimize the alkali metal migration and raster scan mode to reduce the temperature increase were adopted for the measurement, as previously suggested (Goldstein et al., 1992; Pacella et al., 2016). AMS1 was investigated with a Jeol JSM 6400 Scanning Electron Microscope equipped with a windowless Oxford INCA EDS detector. The operating conditions were 15 kV and 1.2 nA, with an electron beam about 1 μm in diameter and low counting time; errors are ±2-5% for major elements and ±5-10% for minor components, while detection limits are 0.1 wt%. The standards used for calibration included Ni, V, Cr_2O_3, $BaSO_4$, CaF_2, $SrTiO_3$, ilmenite, chromite, glass, olivine, augite, microcline, anorthoclase, and apatite. The reliability of the chemical analyses was assessed using a charge balance error formula (E%, Passaglia, 1970), the K-content test (Cametti et al., 2013; Mattioli et al., 2018), and an Mg-content test (Dogan and Dogan, 2008).

2.3. Energy dispersive X-ray fluorescence (EDXRF)

EDXRF analysis was performed using the instrument Epsilon 1 (Malvern Panalytical), equipped with a silver anode (Ag) X-ray tube and a Silicon Drift Detector (SDD) with an energy resolution of <135 eV for Mn-Kα. The analyses were carried out under two different experimental conditions for each sample. The first condition was optimized for the excitation of low-Z elements (Mg to Ca K-lines), using 10 kV, 500 μA, and an acquisition time of 180 s. The second condition was optimized for the excitation of higher-Z elements (V to Zr K-lines and Pb L-lines), using 50 kV, 100 μA, an acquisition time of 300 s, and a Cu filter (500 μm). Quantitative analyses were performed using the proprietary software of the Epsilon 1 system (Malvern Panalytical). Each sample was analyzed in triplicate.

To verify the precision and accuracy of the EDXRF system, elemental analysis of an internal reference standard was also carried out. The reference material samples were prepared under the same experimental conditions as the zeolite samples. All measurements were performed under normal atmospheric conditions at room temperature. The EDXRF spectra were processed using the instrument's proprietary software (Malvern Panalytical). The reference sample was prepared to ensure a flat surface and full irradiation during measurement.

2.4. X-ray powder diffraction (XRPD)

Pure crystals were selected from each sample under a binocular microscope, then carefully disaggregated, finely ground in an agate mortar, and placed in a 0.7 mm side-opened aluminium sample holder. XRPD (X-ray Powder Diffraction) data were collected using a Philips X'Change PW1830 powder diffractometer set at 35 kV accelerating voltage and 30 mA beam current, with CuKα radiation ($\lambda = 1.54506$ Å). Measurements were taken in a Bragg-Brentano geometry from 2° to 65°

at 2Θ, with a 0.01° step size and a 2.5-s count time for each step to ensure high-intensity patterns. The diffractometer used a 1° maximum divergence compensating slit, a 0.2 mm receiving slit, and a graphite crystal monochromator. Semi-quantitative XRPD analysis was also done using X'Pert Quantify and X'Pert HighScore Plus software, with quartz as an internal calibration standard. Peak width variations were minimal (within ±2% of the average value). Each sample was measured three times.

2.5. Cell culture and treatments

This study was performed on the primary cell line of human primary pulmonary fibroblasts MRC-5 (ATCC –CCL-1711 American Type Culture Collection). According to the manufacturer's datasheet, these cells exhibit typical fibroblast morphology. The cells were cultivated in Eagle's Minimum Essential Medium (EMEM) supplemented with 1 % antibiotic (penicillin and streptomycin), 2 mM glutamine, 1 mM sodium pyruvate and 10% fetal bovine serum (FBS). The cells were incubated at 37 °C, in a humid atmosphere of 5% CO_2. At 80% confluence, the cells adherent to the culture substrate were detached by enzymatic treatment with Trypsin-EDTA. Briefly, the MRC-5 cells were seeded and left to adhere for 24 h. The next day, the culture medium was replaced with a fresh one, which contained different zeolite fibers (SC1, AMS1, FER5, MOL1) at concentrations of 150 μg/mL, followed by incubation for 24 or 48 h. After the incubation, the treatment was removed, and the cells were processed for analysis.

2.6. Electron paramagnetic resonance (EPR)

MRC-5 cells were cultured and maintained in standard conditions (37 °C, 5% CO_2). The experimental setup included incubating 8×10^5 cells/mL with CAT16 at concentrations of 0.1 mM, in the presence of zeolite fibers (150 μg/mL) for 2 and 24 h. EPR measurements were conducted using a Bruker EMX Spectrometer at X-band frequency (9.5 GHz). The parameters were set as follows: modulation amplitude of 1 G, Receiver Gain of 5.02×10^3, Time Constant of 20.48 ms, and Conversion Time of 40.96 ms. Spectral accumulations were averaged over three scans to enhance the signal-to-noise ratio. Spectrometer calibration was carried out using DPPH ($g = 2.0036$). EPR spectra were analyzed using double integration to quantify radical concentrations. Hyperfine coupling constants (<A>), correlation times (τ), and line widths (W1) were determined through spectral simulations using the MC Simulation Program (Altenbach, 1995).

2.7. Cell viability

Cells were seeded into 6-well plates (3×10^5/well) and the following day, treatments with the fibrous zeolites were carried out and placed in an incubator at 37 °C and 5% CO_2 for 24 and 48 h. After the treatment, the cells were detached and centrifuged at 1200 rpm for 5 min, and cell viability was assessed by resuspending the cells in an equivalent volume of 0.4% Trypan Blue solution (Sigma-Merk). Finally, the cells were counted with a Burker's chamber and the number of viable cells in the control condition was set as 100%.

2.8. Calcein AM assay

Cell viability was measured by Calcein AM (Thermo Fisher Scientific) assay. Calcein AM is a cell-permeant dye that can be used to determine cell viability in live cells. Live cells with intact cell membranes take up Calcein AM, which is then cleaved by intracellular esterases to produce fluorescent Calcein. Following treatments, MRC-5 cells were incubated with 1 μM Calcein AM at 37 °C for 30 min. At the end of incubation, the cells were observed, and the images were obtained at 485 nm excitation and 538 nm emission using a digital camera-attached fluorescence microscope with data acquisition software (Nikon ECLIPSE TS100, software NIS-Elements F, Nikon Europe BV, Amsterdam). The analysis was performed by ImageJ software analysing 5 images for each experimental condition and the number of viable cells was assessed setting the control condition as 100%.

2.9. Detection of ROS production

Intracellular ROS levels were analyzed with 2′,7′-dichlorofluorescein diacetate (DCFH-DA, Sigma-Aldrich, Milan, Italy), which is a cell-permeable non-fluorescent probe that turns to highly fluorescent 2′,7′-dichlorofluorescein (DCF) upon oxidation. Briefly, cells (1×10^5/well) in 24-well plates were incubated with DCFH-DA (5 μM) for 30 min at 37 °C. The fluorescence emission was analyzed at ex/em 485/520 nm in Spark multimode reader from Tecan.

2.10. Analysis of lysosomal compartment

The cells were seeded in black 96-well plates (approximately 1.5×10^5/well) and subsequently treated for 24 h at 37 °C and 5% CO_2. At the end of the incubation, the medium was removed, and the cells were washed with PBS. The LysoTracker Green DND-26 (LTG, Invitrogen) probe was used at 100 nM for 30 min. Fluorescence intensity was detected at ex/em 485/520 nm and quantified with the FLUOstar OPTIMA plate reader.

2.11. Statistical analyses

Statistical analyses were performed using Prism version 9.00 (GraphPad Software, San Diego, CA, USA). Quantitative data are expressed as mean ± standard deviation (SD) based on at least three independent experiments. Differences between groups were analyzed using a One-way analysis of variance (One-way ANOVA), followed by a Tukey post hoc Test. The value of $p < 0.05$ was indicative of a statistically significant difference.

3. Results

3.1. Morphology and morphometry

The habit of minerals plays a crucial role in their potential health effects. Fibrous zeolites can occur in multiple elongated forms. Erionite, for example, is frequently described in the literature as prismatic, acicular, hair-like, or woolly, occurring as single fibers, fibrils, or bundles. Individual crystals typically range from 2 to 200 μm in length and 0.1 to 10 μm in thickness. Ferrierite and mordenite are generally elongated and fibrous, although not always strongly so, whereas scolecite is prismatic and lacks pronounced fibrous characteristics.

Fig. 1 shows SEM images of the zeolite fibers investigated in this study. The SC1 sample (scolecite) consists of prismatic, elongated crystals with diameters ranging from 0.5 mm to 30 μm and variable lengths (Fig. 1a). These crystals commonly form irregular or radiating clusters and exhibit little to no tendency to split into thin fibers.

In the AMS1 sample (erionite), crystals range from fibrous (needle-like) to highly fibrous, with diameters of 2-5 μm and lengths of 10-100 μm, most frequently between 30 and 40 μm (Fig. 1b). They occur as irregular to parallel bundles up to 100 μm long, with variable thickness. These bundles readily break into individual fibrils as thin as 0.5 μm or less. This sample represents a strongly fibrous form of erionite with a marked tendency to form fibrils.

The FER5 sample (ferrierite) contains flattened, elongated acicular crystals with a highly fibrous, low-flexibility habit (Fig. 1c). Fiber lengths vary from 20 to 300 μm, with an average of 25 μm; approximately half of the fibers are shorter than 20 μm. Fiber widths range from 0.5 to 15 μm, averaging 0.75 μm. More than 80% of the fibers are narrower than 3 μm. This sample reflects a strongly fiber-forming acicular to fibrous ferrierite.

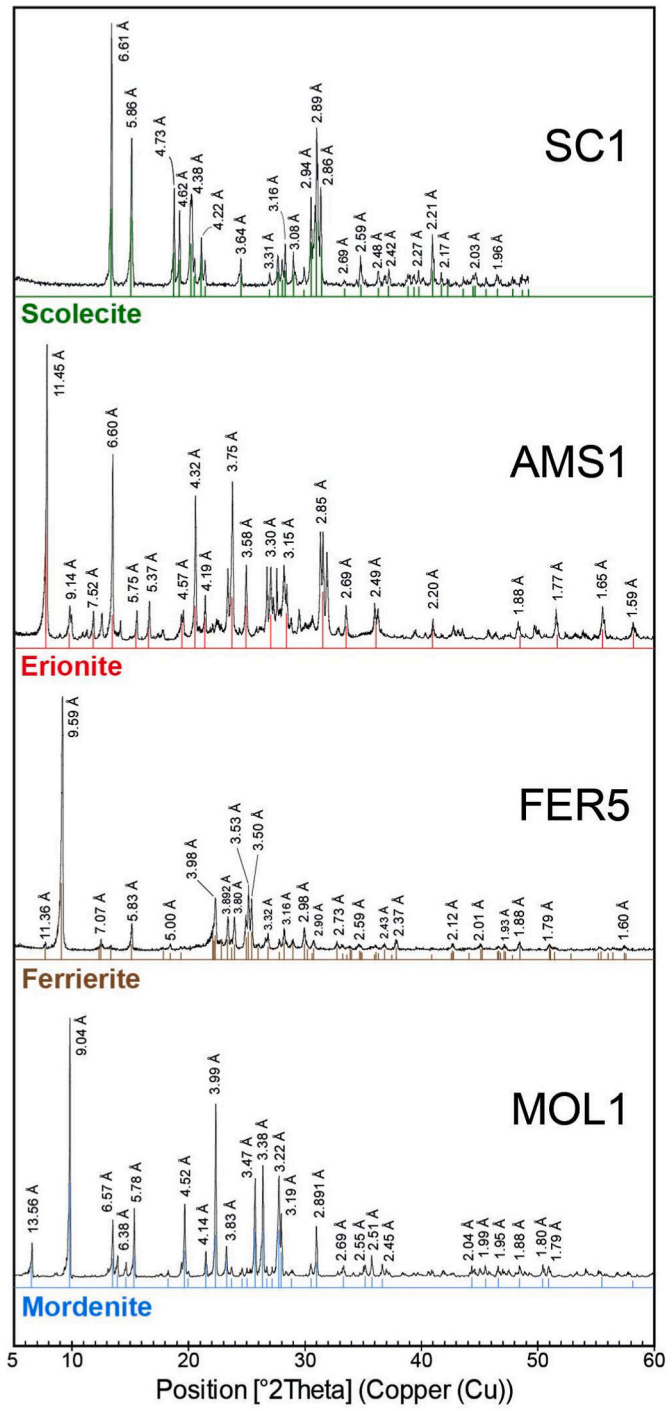

Fig. 2. XRPD patterns of the investigated zeolite fibers.

The MOL1 sample (mordenite) shows roughly prismatic fibrous crystals ranging from 0.5 to 5 mm in length and less than 1 mm in width (Fig. 1d). In some cases, these prismatic structures split into small, rigid fibers and fibrils with average lengths of 100 μm and diameters <0.5 μm. This sample represents moderately fibrous to weakly fiber-forming mordenite.

3.2. Mineralogy

To assess the quality of the separated crystals and exclude the presence of impurities, detailed long-exposure X-ray diffraction (XRPD) analyses were performed on each sample, with exposure times up to 24 h. The resulting diffraction data are shown in Fig. 2.

For the SC1 sample, the XRPD pattern displays all characteristic reflections of pure, highly crystalline scolecite, indexed to a monoclinic cell. The main peaks occur at 6.61 Å, 5.86 Å, and 2.89 Å, with closely spaced reflections in the 30°-31.5° 2-theta range.

The AMS1 sample (erionite) exhibits a dominant primary reflection at 11.45 Å, along with the complete set of minor reflections typical of this zeolite (6.60 Å, 3.75 Å, 4.32 Å, and 2.85 Å). Trace amounts of quartz, clinoptilolite, and feldspar are also detectable.

The diffraction pattern of the FER5 sample corresponds to pure ferrierite, showing a main peak at 9.95 Å and minor reflections at 3.99 Å, 3.53 Å, and 3.50 Å. The low baseline of the pattern indicates high crystallinity.

Similarly, the MOL1 sample (mordenite) demonstrates high crystallinity, as evidenced by a very low background and well-defined reflections at 9.04 Å (main peak) and 3.99 Å (secondary peak), along with minor peaks at 3.38 Å, 3.47 Å, and 3.22 Å.

3.3. Chemical composition

The microchemical compositions (major-, minor- and trace elements) of the investigated zeolite crystals are reported in Table 1. The SC1 and FER5 samples were previously analyzed for major elements (Mattioli et al., 2016, 2022) and are reported here for comparison.

Prismatic scolecite from the SC1 sample is a typical Ca-zeolite with an average chemical formula of $Ca_{5.86}[Al_{14.35}Si_{22.31}O_{80}]\cdot 21.12H_2O$. The Si/(Si + Al) ratio is approximately 0.61, consistent with literature values.

The fibrous erionite (AMS1 sample) can be classified as erionite-K, with an average chemical composition of $(K_{3.20}Na_{3.14}Ca_{0.09}Mg_{0.06})[Al_{7.88}Si_{28.29}O_{72}]\bullet 29.88H_2O$ and a Si/(Si + Al) ratio of 0.78, comparable to erionites from Durkee, Oregon, USA (Passaglia et al., 1998) and Lander County, Nevada, USA (Mattioli et al., 2016; Ballirano et al., 2018). K^+ is the dominant extra-framework cation (average 3.2 *apfu*), followed by Na^+ (average 3.14 apfu), while Ca^{2+} (average 0.09 *apfu*) and Mg^{2+} (0.06 *apfu*) are very low. Trace Fe (up to 0.18 *apfu*) likely reflects surface impurities rather than the crystal structure.

The fibrous ferrierite (FER5 sample) has an average chemical formula of $(Mg_{1.77}K_{0.65}Ca_{0.65}Na_{0.36})[Si_{29.80}Al_{6.20}O_{72}]\bullet 22.76H_2O$, with a Si/(Si + Al) ratio of 0.83. Extra-framework cations follow the trend $Mg^{2+} > (Ca^{2+} \sim K^+)$, while Na^+ is relatively low (average 0.36 apfu).

The fibrous mordenite (MOL1 sample) is Na-rich, with an average composition of $(Na_{3.31}Ca_{2.38}K_{0.17}Mg_{0.06})[Al_{8.98}Si_{39.18}O_{96}]\bullet 28.30H_2O$ and a Si/(Si + Al) ratio of 0.83. The dominant extra-framework cations are Na^+ (average 3.31 *apfu*) and Ca^{2+} (average 2.38 *apfu*), while K^+ (average 0.17 *apfu*) and Mg^{2+} (<0.1 apfu) are minor. This composition aligns with fibrous mordenite from Northern Italy (Giordani et al., 2022a).

Regarding trace elements, in most cases (64%) their concentrations are below the instrument's detection limit. Arsenic was detected, in very small amounts (35.2 ppm), only in fibrous erionite (AMS1). Traces of Ba and Ce were identified in samples SC1 (65 and 247 ppm, respectively) and FER5 (44 and 950.6 ppm, respectively). Co and Li were also detected in minor amounts in scolecite (SC1: 15 and 14 ppm, respectively) and mordenite (MOL1: 22 and 11 ppm, respectively). Rb and Sr were present in all samples, with lower concentrations observed for Rb (71.6, 61.5, 145.2, and 35.8 ppm in SC1, AMS1, FER5, and MOL1, respectively) and higher concentrations for Sr (2510, 411, 7120, and 1680 ppm in SC1, AMS1, FER5, and MOL1, respectively). Fibrous erionite also contains traces of Th (42.5 ppm), Y (89.2 ppm), and Zn (96.4 ppm), while V was detected only in mordenite sample MOL1 (23 ppm). Zr occurs in trace amounts in samples SC1 (9.7 ppm), FER5 (10.4 ppm), and MOL1 (8 ppm), whereas a higher concentration was measured in erionite (332.1 ppm).

Table 1
Chemical compositions (major-, minor- and trace elements) of the investigated zeolite fibers. N, number of points; σ, standard deviation; ΣT sum of cations in tetrahedral sites; Σef sum of cations in extra-framework sites; E% measure of charge balance as defined by Passaglia (1970); [a]Hypothesized water content; [b]Mattioli et al. (2016); [c]Mattioli et al. (2022); *bdl*, below detection limit.

Sample	**SC1**[b]	σ	**AMS1**	σ	**FER5**[c]	σ	**MOL1**	σ
	Average (N = 4)		Average (N = 5)		Average (N = 8)		Average (N = 6)	
SiO_2	48.15	*0.06*	71.68	*0.18*	67.61	*0.15*	66.19	*0.36*
TiO_2	*bdl*	-	0.12	*0.02*	*bdl*	-	*bdl*	-
Al_2O_3	26.28	*0.03*	16.94	*0.21*	11.94	*0.06*	12.87	*0.28*
Fe_2O_3	*bdl*	-	0.61	*0.08*	*bdl*	-	*bdl*	-
MnO	*bdl*	-	0.05	*0.01*	0.01	*0.01*	0.02	*0.01*
MgO	*bdl*	-	0.11	*0.05*	2.70	*0.18*	0.04	*0.04*
CaO	11.80	*0.09*	0.21	*0.09*	1.38	*0.24*	3.49	*0.18*
Na_2O	*bdl*	-	4.09	*0.17*	0.42	*0.23*	2.97	*0.09*
K_2O	*bdl*	-	6.36	*0.11*	1.15	*0.12*	0.25	*0.03*
H_2O	13.67		18.5[a]		14.80		14[a]	
Si	22.31	*0.02*	28.29	*0.10*	29.80	*0.06*	39.18	*0.18*
Al	14.35	*0.01*	7.88	*0.12*	6.20	*0.06*	8.98	*0.2*
ΣT	*36.66*		*36.35*		*36.00*			
Fe	-	-	0.18	*0.05*	-	-	-	-
Mg	-	-	0.06	*0.02*	1.77	*0.10*	0.06	*0.03*
Ca	5.86	*0.05*	0.09	*0.05*	0.65	*0.10*	2.38	*0.11*
Na	-	-	3.14	*0.13*	0.36	*0.21*	3.31	*0.10*
K	-	-	3.20	*0.11*	0.65	*0.09*	0.17	*0.03*
Σef	*5.86*		*6.49*		*3.43*			
H_2O	21.12		29.88		22.76		27.63	
E%			6.88		5.9		7.31	
R	0.61		0.78		0.83		0.81	
As	*bdl*	-	35.2	*0.04*	*bdl*	-	*bdl*	-
Ba	65	*0.02*	*bdl*	-	44	*0.04*	*bdl*	-
Cd	*bdl*	-	*bdl*	-	*bdl*	-	*bdl*	
Ce	247	*0.8*	9	*0.01*	950.6	*12*	*bdl*	-
Co	15	*0.05*	*bdl*	-	*bdl*	-	22	*0.01*
Cr	*bdl*	-	*bdl*	-	*bdl*	-	*bdl*	-
Cu	*bdl*	-	*bdl*	-	*bdl*	-	*bdl*	-
Eu	*bdl*	-	99.2	-	212.5	*1.5*	45.4	*0.7*
Hg	*bdl*	-	*bdl*	-	*bdl*	-	*bdl*	-
Li	14	*0.01*	*bdl*	-	*bdl*	-	11	*0.02*
Ni	*bdl*	-	*bdl*	-	*bdl*	-	*bdl*	-
Pb	*bdl*	-	61.1	-	*bdl*	-	*bdl*	-
Rb	71.6	*0.08*	61.5	*0.7*	145.2	-	35.8	*4*
Sn	*bdl*	-	*bdl*	-	*bdl*	-	*bdl*	-
Sr	2510	*14*	411	*2*	7120	*15*	1680	*11*
Th	*bdl*	-	42.5	*0.5*	*bdl*	-	*bdl*	-
V	*bdl*	-	*bdl*	-	*bdl*	-	23	*0.8*
Y	*bdl*	-	89.2	*0.3*	*bdl*	-	*bdl*	-
Zn	*bdl*	-	96.4	*0.5*	*bdl*	-	*bdl*	-
Zr	9.7	*0.05*	332.1	*0.9*	10.4	*0.04*	8	*3*

3.4. EPR interaction

The spectral intensity, measured as double integration of the EPR absorption spectra, varied notably across the fiber samples. Table 2 reports the hyperfine coupling constants, correlation times, and line widths. Fig. 3a shows experimental and simulated EPR spectra of the CAT16+MRC-5+SC1 sample after 2 h of incubation, whereas Fig. 3b illustrates the EPR spectra recorded after 2 h of incubation of the AMS1, SC1 and FER5 zeolites with MRC-5 cells and the CAT16 probe.

After 2 h, Trypsin appears to aid probe solubilization within the system. Fibers + probe samples (CAT16) show lower spectral intensities than the probe-only control (BN, Fig. 4). This reduction is caused by spin-spin interactions between the probe and the fibers, which are weaker in FER5 than in SC1 and AMS1Trypsin. In samples containing both fibers and MRC-5 cells, the spectral intensity is even lower, likely because the probe enters the cellular cytosol and interacts with intracellular antioxidants.

After 24 h, the trend notably changes (Fig. 4). Probe + fiber samples now show higher intensities than the Trypsin control, and higher than their own 2-h values, indicating improved probe solubilization, particularly CAT16, over time. This is consistent with a gradual breakup of initial CAT16 aggregates, which were EPR-silent in the cell membrane at 2 h due to poor membrane solubility. By contrast, fiber + cell samples show reduced intensity, likely due to strong spin-spin interactions. In the controls, solubilization steadily increases over time, except when CAT16 is combined with cells, where the intensity falls because the probe enters the cytosol and is degraded by cellular antioxidants. Notably, SC1 exhibits a slight intensity increase over 24 h, possibly due to fiber-assisted probe delivery at the cell-solution interface. In contrast, AMS1 shows a decline in intensity over time, suggesting greater probe uptake into cells and stronger quenching effects.

Figs. 5 and 6 show the FAST and BROAD spectral components over time, and the evolution of the correlation time across the different zeolite fibers, respectively. The hyperfine coupling constant (<A>) describes the micropolarity around the spin probe. The FAST component shows nearly unchanged micropolarity under all conditions, suggesting a stable local environment. In contrast, the BROAD component, which reflects interaction effects, displays distinct behavior. In particular, AMS1 shows a clear increase in micropolarity from 2 to 24 h, indicating progressively fiber-membrane interactions. In contrast, SC1 and FER5 exhibit a decrease in micropolarity over the same time. In MRC-5 + fiber + CAT16 samples, micropolarity remains consistently lower than in the reference controls for all zeolite types. The correlation time (τ), which reflects microviscosity and interaction strength, is significantly

Table 2
Hyperfine coupling constants (<A> in Gauss), correlation time (τ) and linewidths (W1) determined through MC spectral simulations program of different components (FAST and BROAD).

	<A> (G) FAST	*Error A_fast*	<A> (G) BROAD	*Error A_broad*	τ(ns) FAST	*Error τ_fast*	τ(ns) BROAD	*Error τ_broad*	Intensity (a. u.)	*Error Int.*
AMS1 MRC/5 CAT16 trips 2h	16.83	*±0.084*	16.32	*±0.326*	0.418	*±0.033*	6.61	*±0.331*	27311.90	*±1365.59*
AMS1 MRC/5 CAT16 trips 24h	16.86	*±0.084*	16.55	*±0.331*	0.353	*±0.028*	6.94	*±0.347*	24264.00	*±1213.20*
FER5 MRC/5 CAT16 trips 2h	16.85	*±0.084*	16.61	*±0.332*	0.432	*±0.035*	7.86	*±0.393*	19802.10	*±990.10*
FER5 MRC/5 CAT16 trips 24h	16.86	*±0.084*	16.36	*±0.327*	0.367	*±0.029*	6.95	*±0.348*	25779.73	*±1288.98*
SC1 MRC/5 CAT16 trips 2h	16.84	*±0.084*	16.50	*±0.330*	0.457	*±0.037*	7.62	*±0.381*	23466.81	*±1173.34*
SC1 MRC/5 CAT16 trips 24h	16.84	*±0.084*	16.42	*±0.328*	0.353	*±0.028*	6.45	*±0.323*	26437.51	*±1321.87*
Bn CAT16 2h	16.83	*±0.084*	16.75	*±0.335*	0.211	*±0.017*	2.56	*±0.128*	35678.24	*±1783.91*
Bn CAT16 24h	16.86	*±0.084*	16.65	*±0.333*	0.213	*±0.017*	2.37	*±0.119*	40291.24	*±2014.56*
Bn CAT16 SC1 2h	16.82	*±0.084*	16.84	*±0.337*	0.240	*±0.019*	2.48	*±0.124*	27493.18	*±1374.65*
Bn CAT16 SC1 24h	16.85	*±0.084*	16.84	*±0.337*	0.233	*±0.019*	2.44	*±0.122*	35151.46	*±1757.57*
Bn CAT16 AMS1 2h	16.84	*±0.084*	16.75	*±0.335*	0.205	*±0.016*	2.46	*±0.123*	28876.41	*±1443.82*
Bn CAT16 AMS1 24h	16.84	*±0.084*	16.76	*±0.335*	0.218	*±0.017*	2.49	*±0.125*	43683.61	*±2184.18*
Bn CAT16 Fer5 2h	16.81	*±0.084*	17.22	*±0.344*	0.304	*±0.024*	2.96	*±0.148*	24804.13	*±1240.20*
Bn CAT16 Fer5 24h	16.86	*±0.084*	16.71	*±0.334*	0.205	*±0.016*	2.44	*±0.122*	31563.66	*±1578.18*
Bn CAT16 Trips 2h	16.82	*±0.084*	16.71	*±0.334*	0.189	*±0.015*	2.42	*±0.121*	47554.17	*±2377.70*
Bn CAT16 Trips 24h	16.85	*±0.084*	16.84	*±0.337*	0.214	*±0.017*	2.41	*±0.121*	32668.35	*±1633.41*
Bn CAT16 Trips SC1 2h	16.85	*±0.084*	16.68	*±0.334*	0.191	*±0.015*	2.37	*±0.119*	30666.25	*±1533.31*
Bn CAT16 Trips SC1 24h	16.84	*±0.084*	16.73	*±0.335*	0.202	*±0.016*	2.37	*±0.119*	34289.46	*±1714.47*
Bn CAT16 Trips AMS1 2h	16.85	*±0.084*	16.65	*±0.333*	0.205	*±0.016*	2.42	*±0.121*	30926.28	*±1546.31*
Bn CAT16 Trips AMS1 24h	16.88	*±0.084*	16.71	*±0.334*	0.104	*±0.008*	2.16	*±0.108*	35825.51	*±1791.27*
Bn CAT16 Trips FER5 2h	16.83	*±0.084*	16.72	*±0.334*	0.191	*±0.015*	2.37	*±0.119*	39705.80	*±1985.29*
Bn CAT16 Trips FER5 24h	16.86	*±0.084*	16.59	*±0.332*	0.189	*±0.015*	2.36	*±0.118*	35573.01	*±1778.65*
Bn CAT16 MRC/5 2h	16.83	*±0.084*	16.76	*±0.335*	0.223	*±0.018*	2.91	*±0.146*	25806.89	*±1290.34*
Bn CAT16 MRC/5 24h	16.86	*±0.084*	16.72	*±0.334*	0.188	*±0.015*	2.61	*±0.131*	24660.22	*±1233.01*

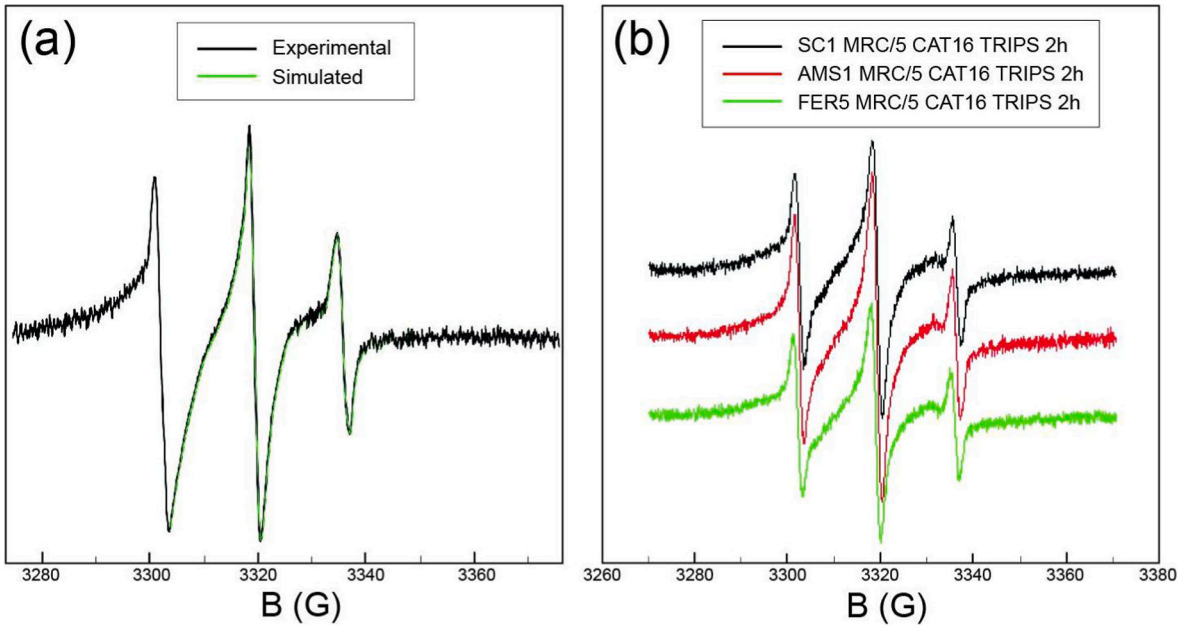

Fig. 3. (a) Experimental (black) and simulated (green) EPR spectra of CAT16+MRC-5+SC1 sample after 2 h of incubation. The best fit simulation consists of 20.47% FAST component ($\boldsymbol{\tau} = 457$ ps) and 79.53% BROAD component ($\boldsymbol{\tau} = 7.62$ ns). (b) EPR spectra recorded after 2 h of incubation of AMS1, SC1 and FER5 zeolites with MRC-5 cells and CAT16 probe. (For interpretation of the references to color in this figure legend, the reader is referred to the Web version of this article.)

higher in all samples compared to controls. The BROAD component shows values around 7 ns - much longer than the FAST component -

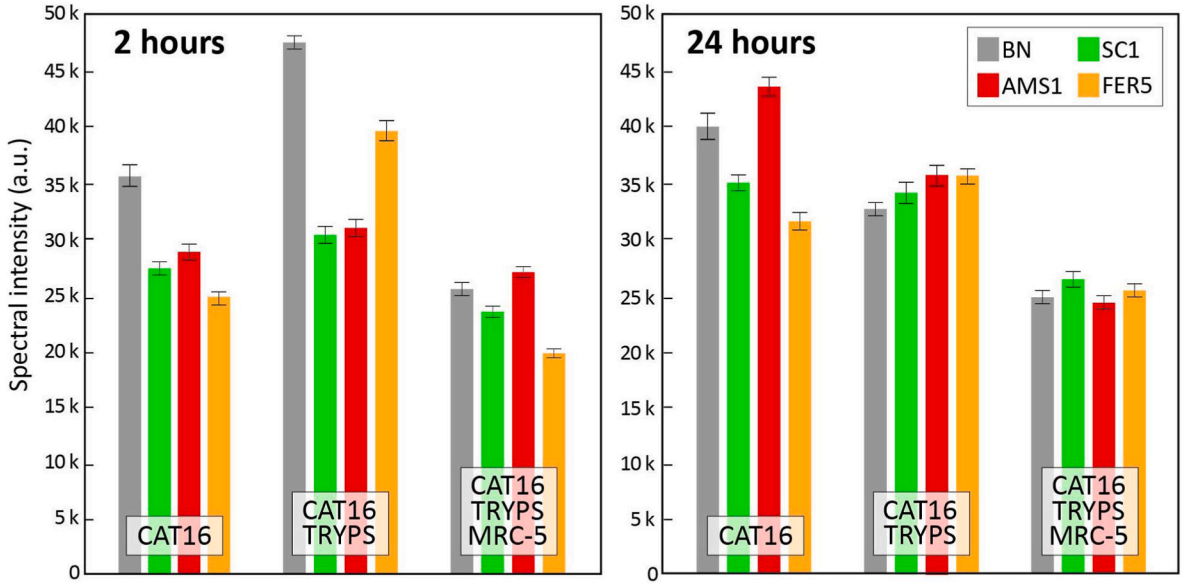

Fig. 4. EPR spectral intensity over time.

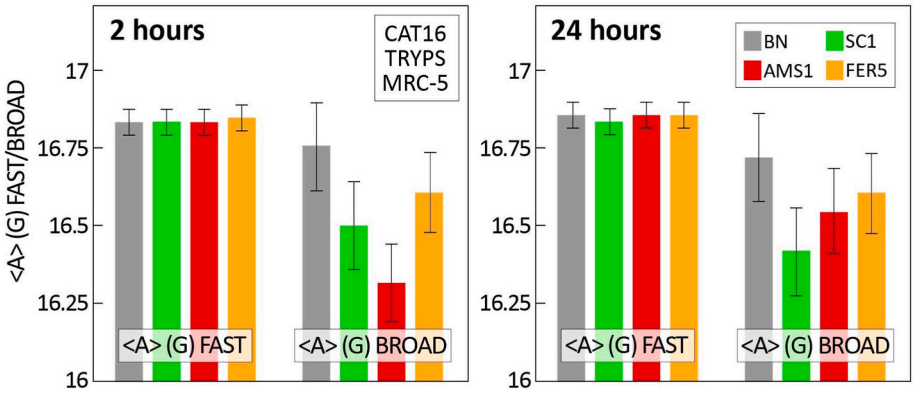

Fig. 5. Hyperfine coupling constant of FAST and BROAD components at different interaction time.

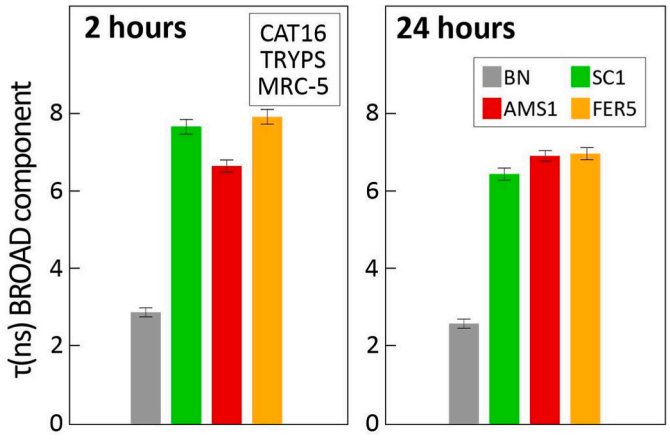

Fig. 6. Correlation time (τ) across different zeolite fibers (graph showing τ for SC1, AMS1, and FER5 at 2 h and 24 h, for BROAD component).

confirming its stronger interaction with the surrounding environment. For SC1 and FER5, τ values are high at 2 h but decrease at 24 h, suggesting rapid early interactions followed by stabilization. In contrast, AMS1 shows an increase in τ at 24 h, indicating rising microviscosity and progressively stronger interactions with the cellular membrane.

The percentage of the BROAD component increases over time in all control samples, consistent with improved solubilization and more uniform distribution of CAT16. In MRC-5 + CAT16 + AMS1 and MRC-5 + CAT16 + SC1 samples, the rising BROAD component similarly indicates progressive probe solubilization and incorporation into the cell membrane. This incorporation likely involves the probe orienting with the polar heads on the membrane surface and interacting with adjacent phospholipid groups. In contrast, FER5 shows a high BROAD percentage already at 2 h, likely due to early probe aggregation.

The FAST component, associated with free radical groups at the outer or inner cell membrane surface, shows higher polarity than the BROAD component. Spectral analysis highlights clear differences in probe behavior between zeolites and reference controls. The BROAD component consistently exhibits higher microviscosity when fibers are present, indicating stronger probe–membrane interactions. The hyperfine coupling constant (<A>) decreases slightly over time for FER5, suggesting reduced micropolarity, while SC1 remains nearly unchanged. Controls, by comparison, show greater variability in <A> values, reflecting a more dynamic environment. Correlation times (τ) further differentiate the zeolites. All fiber samples show higher τ values than controls. SC1 and FER5 display high τ at 2 h that declines by 24 h, suggesting early interactions followed by stabilization. Conversely, AMS1 maintains elevated τ values throughout the experiment,

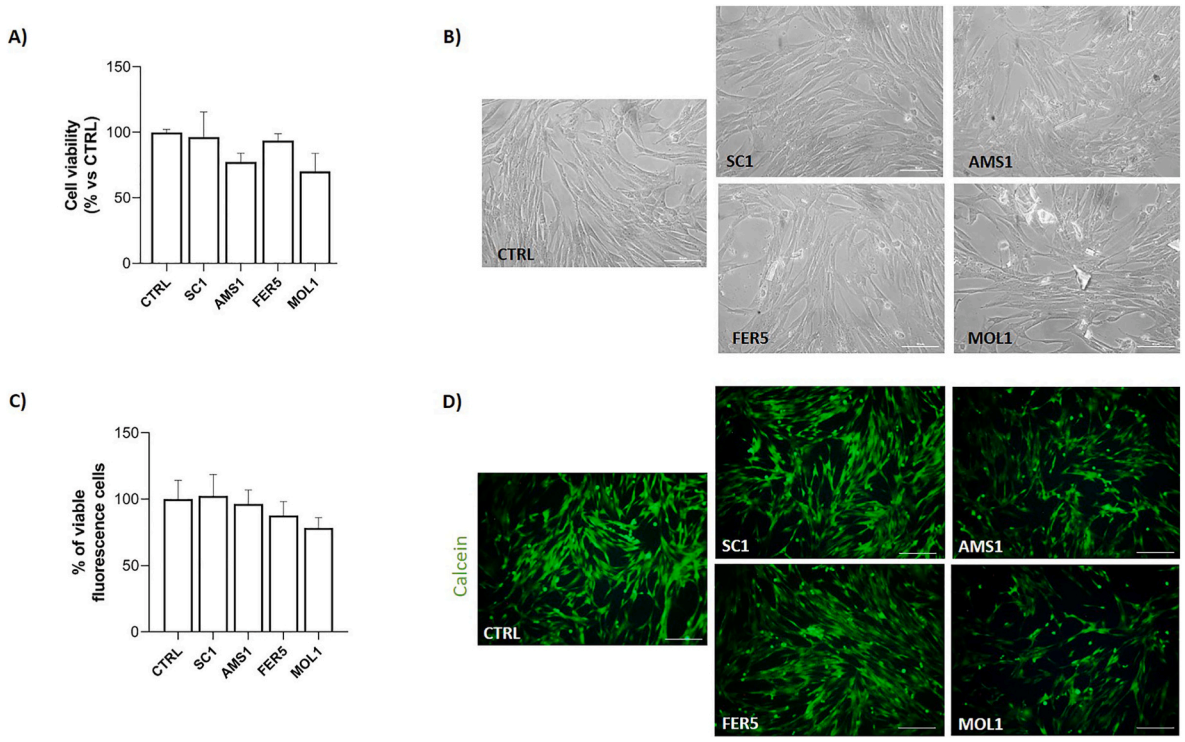

Fig. 7. Effect of zeolite fibers on human pulmonary MRC-5 cell viability after 24 h of treatment. (A) The graph illustrates the percentage of cell viability after 24 h of treatment with the four fibrous zeolites, SC1, AMS1, FER5, and MOL1, at a concentration of 150 μg/mL. Each value is expressed as a percentage ± SD (N = 3 independent experiments. (B) Representative bright field microscopy images of MRC-5 control cells and MRC-5 treated with SC1, AMS1, FER5 and MOL1 fibrous zeolites after 24 h of treatment. Scale bar 100 μm. (C) The graph shows the percentage of Calcein AM-labelled cells after 24 h of treatment with the fibrous zeolites SC1, AMS1, FER5 and MOL1 at the concentration of 150 μg/mL. (D) Representative fluorescence images of MRC-5 control cells and MRC-5 treated with SC1, AMS1, FER5 and MOL1 labelled with Calcein AM. Scale bar 100 μm.

indicating sustained membrane interactions and increased microviscosity.

Finally, spectral line width (W1) analysis shows that AMS1 and FER5 have broader lines than SC1 and controls, reflecting stronger spin-spin interactions and more robust probe binding. Overall, the data confirm that zeolite fibers influence MRC-5 cells within just 2 h of exposure, with each fiber type showing distinct interaction dynamics.

These EPR findings, which reflect distinct modes and strengths of fiber–membrane interactions, are consistent with the biological results observed in MRC-5 fibroblasts. Notably, the EPR response cannot be interpreted solely in terms of interaction amplitude. The modest spectral changes observed for scolecite likely reflect a weak or transient membrane perturbation, whereas the more pronounced motional restriction induced by erionite suggests a more persistent alteration of membrane organization, which may be relevant to the observed cytotoxic effects.

The associated alterations in membrane polarity and microviscosity suggest that fiber exposure compromises cellular integrity and likely contributes to the cytotoxic and oxidative effects discussed in the following sections.

3.5. *Effect of zeolite fibers on human pulmonary MRC-5 cell viability*

To assess the potential toxicity of zeolite fibers (SC1, AMS1, FER5 and MOL1) on MRC-5 cells, we initially performed cell viability assays after 24 h of exposure at various fibers concentrations (1.5, 15, 150 μg/mL; Supplementary Fig. 1A and B). Based on the results and on previous studies (Cangiotti et al., 2018; Timblin et al., 1998; Mirata et al., 2022), we selected a concentration of 150 μg/mL and evaluated cell viability by Trypan Blue and the Calcein AM assays after 24 and 48 h of exposure. Cell viability was evaluated using Trypan Blue and the Calcein AM assays. As shown in Fig. 7, no significant toxicity was detected after 24 h for any fiber type. A slight reduction of cell viability was observed in cells exposed to AMS1 and MOL1 (Fig. 7A). Bright-field images confirmed the presence of extracellular mineral fibers, while cells largely maintained their characteristic elongated morphology. A minor reduction in cell density was visible in AMS1-and MOL1-treated samples (Fig. 7B). Besides, the quantitative and qualitative assessment of MRC-5 viability by Calcein AM staining further supported these findings, showing viability values comparable to untreated controls (Fig. 7C). However, a small decrease in the percentage of Calcein AM-labelled cells was noted in the MOL1 sample (Fig. 7C and D).

Because the 24 h viability assessment showed no significant toxicity, we extended the exposure to 48 h (Fig. 8). At this time point, Trypan Blue staining reveals a marked decrease in cell viability, approximately 50%, in cells exposed to AMS1, FER5 and MOL1 ($p < 0.05$ and $p < 0.01$) compared to control condition (Fig. 8A). In contrast, SC1 did not reduce viability, showing values comparable to the untreated sample. Optical microscopy confirmed these findings, showing increased numbers of floating cells and reduced cell density in AMS1-, FER5-and MOL1-treated samples, whereas SC1-treated cells displayed morphology similar to controls, with floating and more well-spread adherent cells (Fig. 8B).

Calcein AM staining further supported these results: FER5 and MOL1 reduced viable cell percentages by ~25% (***$p < 0.001$ *vs* Ctrl), while AMS1 induced a stronger effect with ~50% viability loss (****$p < 0.0001$ *vs* Ctrl) (Fig. 8C). Fluorescent microscopy likewise showed visible fewer bright green fluorescent cells in AMS1-, FER5-and MOL1-treated samples compared to both control and SC1 conditions (Fig. 8D).

3.6. *Zeolite fibers induce intracellular ROS production in the human MRC-5 pulmonary fibroblast cell line*

To assess ROS production, MRC-5 cells were labelled with the fluorogenic dye DCFH-DA. As shown in Fig. 9A, AMS1, FER5, and MOL1

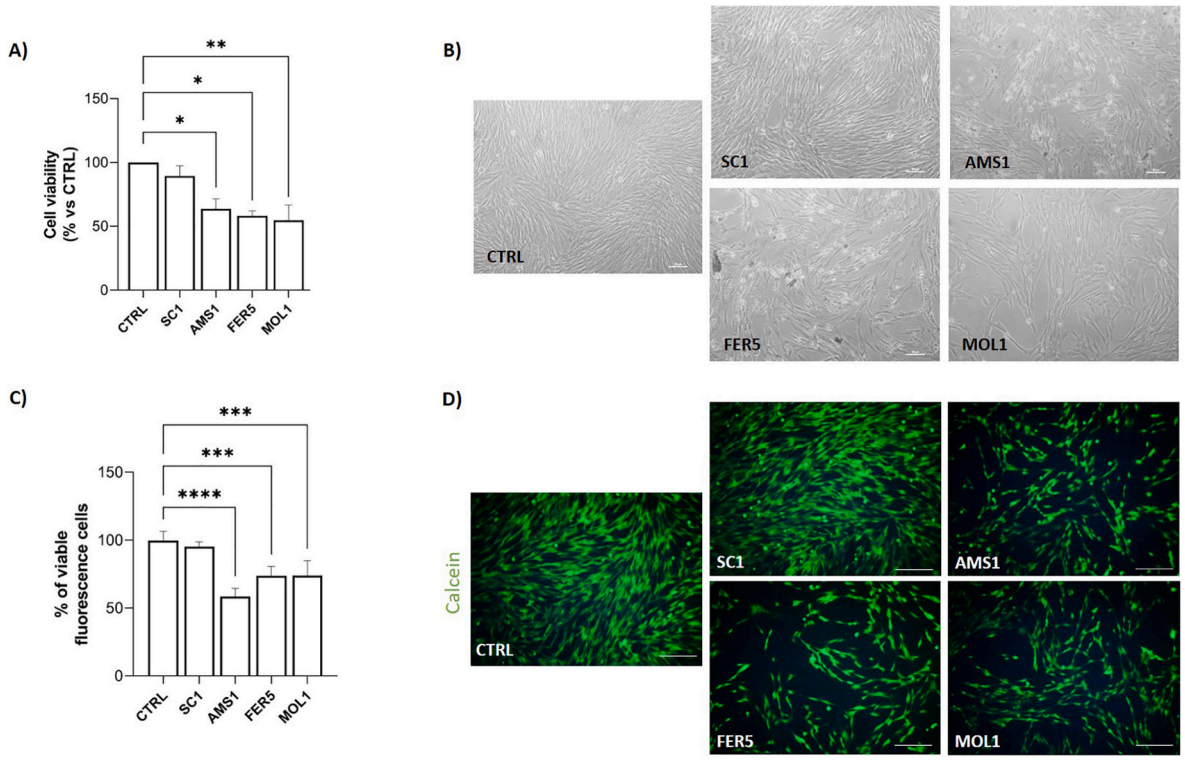

Fig. 8. Effect of zeolite fibers on human pulmonary MRC-5 cell viability after 48 h of treatment. (A) The graph depicts the percentage of cell viability after 48 h of treatment with the four fibrous zeolites SC1, AMS1, FER5 and MOL1 at a concentration of 150 μg/mL. Each value is expressed as a percentage ± SD (N = 3 independent experiments; *$p < 0.05$, **$p < 0.01$ vs Ctrl). (B) Representative bright field microscopy images of MRC-5 control cells and MRC-5 treated with SC1, AMS1, FER5 and MOL1 fibrous zeolites after 48 h of treatment. Scale bar 100 μm. (C) The graph shows the percentage of Calcein AM-labelled cells after 48 h of treatment with the fibrous zeolites SC1, AMS1, FER5 and MOL1 at a concentration of 150 μg/mL. Each value is expressed as a percentage ±SD; ***$p < 0.001$, ****$p < 0.0001$ vs Ctrl. (D) Representative fluorescence images of MRC-5 control cells and MRC-5 treated with SC1, AMS1, FER5 and MOL1 labelled with Calcein AM. Scale bar 100 μm.

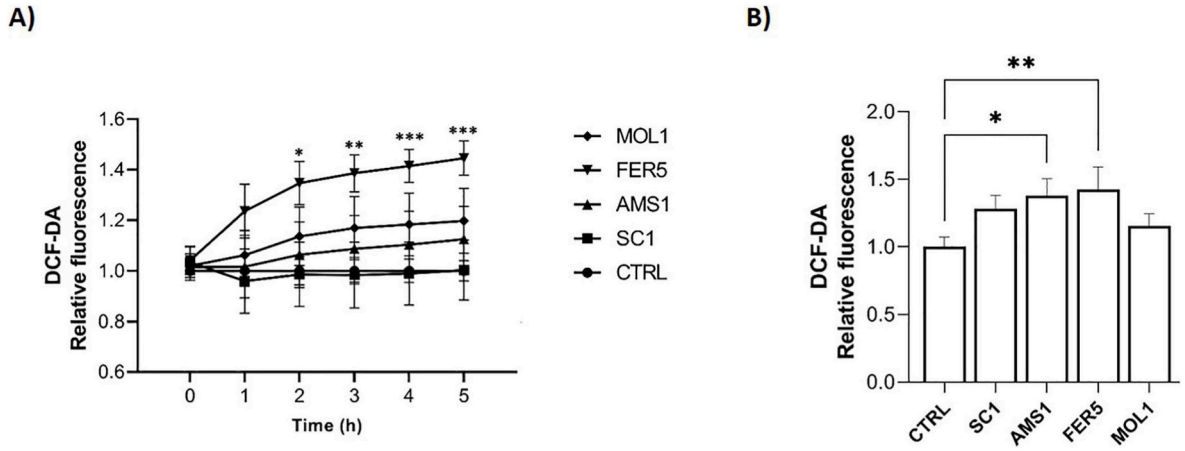

Fig. 9. Evaluation of intracellular ROS production in MRC-5 treated with zeolite fibers. (A) Intracellular ROS production was measured by DCF-DA analysis in MRC-5 cells incubated for 5 h in the presence or absence of 150 μg/mL of mineral fibers SC1, AMS1, FER5, and MOL1. Results are expressed as the relative fluorescence of ROS production compared to the untreated control and represent the mean ± SD of three experiments (*$p < 0.05$, **$p < 0.01$, ***$p < 0.001$). (B) Intracellular ROS production in MRC-5 cells incubated for 24 h in the presence or absence of 150 μg/mL of mineral fibers SC1, AMS1, FER5 and MOL1. *$p < 0.05$, **$p < 0.01$, respectively.

administration to MRC-5 cells induced an early increase in intracellular ROS, with oxidation levels rising progressively over the first 5 h of treatment. In particular, FER5 fiber triggered the strongest response (approximately 1.4-fold increase), followed by MOL1 and AMS1. In contrast, SC1 did not affect ROS production in MRC-5, maintaining levels comparable to the control condition (Fig. 9A). We next examined the alteration of oxidative intracellular state after 24 h of exposure (Fig. 9B). Zeolite fibers continued to stimulate ROS production over this longer time. Notably, AMS1 and FER5 caused a significant increase in intracellular ROS levels (approximately 1.5-fold; $p < 0.05$ and $p < 0.01$, respectively) compared to the control.

3.7. Alteration of lysosome content induced by zeolite fibers

To investigate potential alteration in the lysosomal compartment, a key system for degrading exogenous materials such as fibrous zeolites, as

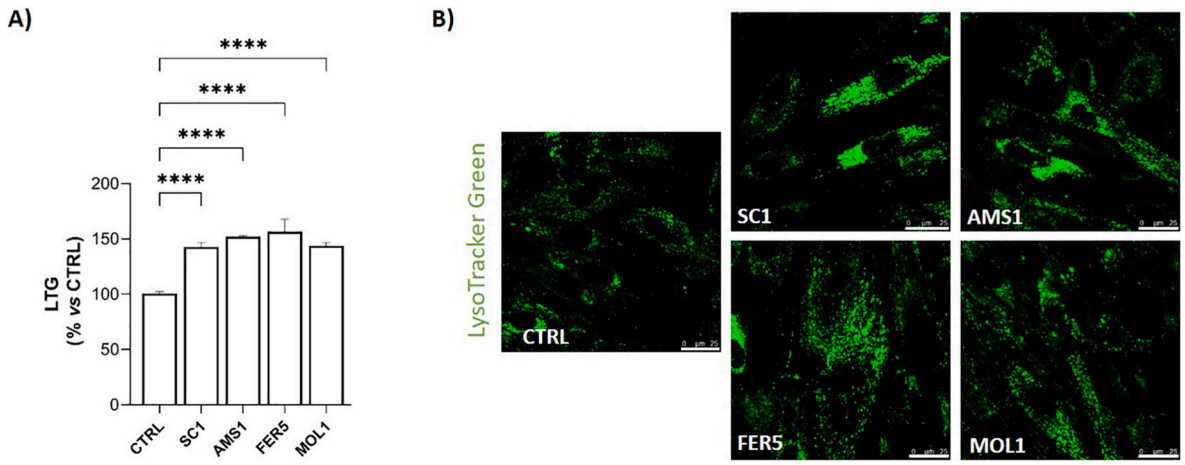

Fig. 10. Lysosomal compartment assessment in MRC-5 treated with zeolite fibers. (A) Intracellular lysosomal content was measured by LysoTracker Green (LTG) in MRC-5 cells after 24 h in the presence or absence of 150 μg/mL of mineral fibers SC1, AMS1, FER5, and MOL1. Results are expressed as a percentage of lysosomes compared to the untreated control and are the mean ± SD (N = 3 independent experiments; ****$p < 0.0001$). (B) Representative confocal images of MRC-5 cells labelled with LTG in the presence or absence of mineral fibers SC1, AMS1, FER5 and MOL1 for 24 h. Scale bar 25 μm. (For interpretation of the references to color in this figure legend, the reader is referred to the Web version of this article.)

well as damaged cellular components, we assessed lysosomal activity using LysoTracker Green (LTG). The statistical histogram showed that LysoTracker Green (LTG) fluorescence intensity (Fig. 10A) was greater in MRC-5-treated cells than in their normal counterparts (approximately 50% increase ±SD; $p < 0.0001$), indicating a wider number of acidic vesicular organelles induced by the exposure to all fibers. Confocal microscopy (Fig. 10B) confirmed these findings, revealing a higher accumulation of acidic vacuoles in fiber-treated cells, evidenced by an increased number of bright fluorescent green puncta compared to the accumulation occurring in normal cells.

4. Discussion

Several factors determine how mineral fibers affect human health, particularly their toxicity and carcinogenicity. The most significant include particle size and shape, specific surface area, chemical composition, Si/Al ratio, biosolubility, and the presence of surface impurities, metals, and radioactive elements (Sanchez et al., 2009; Wylie et al., 2020; Korchevskiy and Wylie, 2021; Gualtieri, 2023; Giordani et al., 2022c, 2025). Because the fibers, fibrils, elongated mineral particles, and cleavage fragments in the investigated fibrous zeolites are very small, at least a fraction - depending on the mineral species - is likely small enough to be inhaled and reach the respiratory system. Erionite (AMS1) shows the smallest fiber size and a strong tendency to fragment into even thinner fibers. Ferrierite (FER5) also splits into small fibers, though less efficiently and with generally larger dimensions. Mordenite (MOL1) forms fibers less readily, while scolecite (SC1) shows minimal to no tendency to develop thin fibers. Thus, the relative abundance of potentially inhalable fibers in the studied samples is: AMS1 > FER5 > MOL1 > SC1.

The degree of fibrosity is closely linked to the crystal's surface area available for interaction with biological systems. The SC1 sample has a specific surface area (SSA) of 1.5 m^2/g and a total pore volume of 0.007 mL/g. Of this volume, 43% corresponds to pores larger than 80 nm, 34% falls within the 20-80 nm range, and 21% consists of pores smaller than 20 nm (Mattioli et al., 2016). Literature reports a wide range of BET-derived SSA values for erionite. Some studies report SSA values between 8 and 30 m^2/g (Mattioli et al., 2016; Giordani et al., 2022c; Pollastri et al., 2014), while others document much higher values (Aguilar-Armenta and Patiño-Iglesias, 2002; Ballirano et al., 2015; Passaglia, 1970; Mertens et al., 2009). For ferrierite, Gualtieri et al. (2018b) recently measured SSA values of 11 m^2/g and 7 m^2/g for natural fibrous samples from Canada and Nevada (USA), respectively. Mordenite generally shows higher SSA values, ranging from 16 m^2/g for fibrous samples (Lycourghiotis et al., 2018) to 19 m^2/g or more when other mineral phases are present (Hernández et al., 2000; Vasylechko et al., 1999; Korkuna et al., 2006). In summary, although SSA in zeolites can vary substantially depending on experimental conditions, accessory minerals, and fiber aggregation, erionite consistently shows the highest SSA among fibrous zeolites, while scolecite has the lowest. Ferrierite and mordenite occupy an intermediate range.

From a mineralogical perspective, the investigated samples consist of pure zeolite phases, with only minor impurities detected in the AMS1 erionite sample (Fig. 2). Their chemical compositions closely match values reported in the literature and are representative of each species. The Si/Al ratio, a key parameter controlling zeolite solubility, follows the sequence: FER5 (4.81) > MOL1 (4.36) > AMS1 (3.59) > SC1 (1.56). Notably, because higher Si/Al ratios than erionite are associated with greater stability under acidic or neutral conditions, such as those in the lung, ferrierite and mordenite are expected to be more biopersistent than erionite (Hartman and Fogler, 2007; Giordani et al., 2019; Di Giuseppe, 2020). Conversely, scolecite, with the lowest Si/Al ratio, is likely to have a faster dissolution rate.

In general, the presence of potentially toxic elements (PTEs; e.g., Fe, Cr, Ni, Mn, Co, and Pb) as impurities and/or within the structure of inhalable fibres, together with the other parameters mentioned above, represents an additional concern in the context of mineral toxicity (e.g., Bloise et al., 2016, 2020; Gualtieri et al., 2018a,b). When inhaled, asbestos and erionite fibres may dissolve in the lungs after a latency period, releasing their toxic constituents and potentially leading to cellular damage (Wei et al., 2014; Pacella et al., 2021, 2023). Extensive evidence has shown that toxic elements, even at low concentrations, can induce significant cellular oxidative stress by increasing the production of reactive oxygen species (ROS) and, in some cases, by causing DNA damage through direct binding (IARC, 2012; Chen et al., 2012; Scharf et al., 2014). In the case of the fibrous zeolites investigated in this study, chemical analyses revealed extremely low or negligible trace element contents. Most importantly, no significant presence of potentially toxic elements (PTEs) was detected. Co, Cr, and Cu were consistently below or only slightly above the detection limits, as were Hg, Ni, and Pb. V and Zn were detected in two samples, but always at very low concentrations. Mn concentrations were also consistently very low, while Fe, an element still considered to have significant toxicity potential, was detected only in fibrous erionite even if in relatively low amounts (0.6 wt%). For these reasons, a toxic effect related to these elements cannot be excluded, as already widely discussed in the scientific literature.

To better understand the processes occurring at the fiber surface and the fiber/cell interface, EPR measurements were performed. These experiments provide detailed insight into the interactions between fibrous zeolites and radical probes, as well as between fibers and cells. In recent years, EPR has become an essential technique for studying such interactions, yielding key information on solubilization, micropolarity, and microviscosity, among other factors (e.g., Gualtieri et al., 2018a,b; Cangiotti et al., 2017, 2018; Mattioli et al., 2016, 2022; Giordani et al., 2022b; Pugnaloni et al., 2023). In this study, EPR revealed marked differences in interaction responses between (i) the zeolite samples and the CAT16 probe and (ii) the zeolite samples and pulmonary fibroblasts. Data for MOL1 were excluded due to interference from minor Fe and Mn impurities in mordenite crystals, as confirmed by ICP-MS analysis, which distort the EPR signal and hinder spectral interpretation. For the other zeolites, EPR analysis demonstrated that interaction of CAT16 with zeolite fibers produced clear spectral changes, reflecting different levels of cellular interaction. AMS1 displayed the strongest response, with the highest spectral intensity and prolonged correlation times. These findings correlate with the reduced cell viability observed in AMS1-treated samples, suggesting that these fibers more effectively disrupt cellular integrity than FER5 and SC1-treated samples, particularly after 48 h of exposure. In AMS1, the progressive decrease in hyperfine coupling constants (<A>) over 24 h points to a change in the micropolar environment, likely linked to oxidative stress induced by the fibers. At the same time, the continued increase in correlation times (τ) suggests a more rigid, less fluid membrane environment, supporting the hypothesis of membrane rigidity and disruption. These effects are likely driven by the surface properties of AMS1, which enhance its interaction with the cellular microenvironment. By contrast, SC1 and FER5 showed decreases in both <A> and τ values over time, suggesting weaker interactions and possible stabilization within the cellular environment. Thus, while SC1 and FER5 display milder and potentially self-limiting interactions, AMS1 maintains a strong and progressively intensifying interaction with cell membranes, consistent with its higher cytotoxic potential. This observation supports the view that membrane engagement alone is not sufficient to predict cytotoxicity, which likely depends on the persistence and the biophysical impact of the fiber-membrane interaction. These findings are consistent with previous studies, which reported that erionite (both fibrous and prismatic) and ferrierite exhibit stronger interaction capabilities than other fibrous zeolites such as mesolite, thomsonite, offretite, and scolecite (Cangiotti et al., 2017, 2018; Gualtieri et al., 2018a,b; Mattioli et al., 2022; Giordani et al., 2022b).

A comprehensive evaluation of the morphological and structural features of the studied fibrous zeolite systems, compared with the findings of Cangiotti et al. (2018), provides meaningful insights despite the use of different cell lines. Both studies underscore the critical role of fiber morphology in driving toxicity. In particular, the fibrous nature of erionite (AMS1), ferrierite (FER5), and mordenite (MOL1) strongly influences their interactions with cellular components. Cangiotti et al. (2018) reported the formation of fiber aggregates and their subsequent internalization into the cytoplasm and even the nucleus of U937 monocyte cells. Fibrous zeolites showed variations in the hyperfine coupling constant (<A>): erionite (AMS1) and ferrierite (FER5) exhibited lower (<A>) values, indicating reduced membrane polarity during interaction, consistent with a more hydrophobic microenvironment that could favor fiber insertion into the lipid bilayer. In contrast, scolecite (SC1) displayed higher <A> values, suggesting weaker membrane perturbation and aligning with its lower cytotoxicity in both studies. Furthermore, AMS1 and FER5 fibers induced a marked decrease in correlation time (τ), consistent with increased microviscosity caused by strong fiber-lipid bilayer interactions. The broadening of line width (W1) observed for AMS1 and FER5 further supports their strong engagement with cellular components, potentially triggering oxidative stress and inflammatory responses. In contrast, SC1 produced only minor changes in τ and W1, in agreement with its comparatively lower cytotoxicity.

The present study also reveals increased intracellular production of reactive oxygen species (ROS) and lysosomal alterations on MRC-5 fibroblasts, particularly following exposure to AMS1, FER5, and MOL1. All fibrous zeolites were found to interact with lung fibroblasts, inducing alterations in the lysosomal compartment after 24 h of exposure. Lysosome-mediated endocytosis is known to play a central role in the cellular uptake and degradation of zeolite fibers, where lytic enzymes facilitate their digestion to maintain cellular homeostasis. However, this process is strongly influenced by fiber size and structure: when fibers are too large to be fully degraded, lysosomal and autophagic dysfunction can occur, leading to intracellular accumulation and triggering a potentially chronic inflammatory response. These findings are consistent with those of Ballirano et al. (2025), who demonstrated that phagocytosis of erionite by THP-1 macrophages causes substantial sequestration of hydronium ions from lysosomes, resulting in rapid pH dysregulation. This is counteracted by hyperactivation of ATP-dependent proton pumps, with consequent energy depletion and mitochondrial dysfunction, ultimately leading to ROS and reactive nitrogen species (RNS) overproduction and oxidative stress. In our study, all tested fibrous zeolites induced elevated intracellular ROS levels for up to 24 h of exposure, with FER5 provoking a response comparable to that of erionite (AMS1). This agrees with Gualtieri et al. (2018b), who reported that erionite and ferrierite share similar chemical and physical properties and may occur as asbestiform fibers capable of triggering toxic processes. Although ferrierite does not contain structural iron, it may carry iron impurities on the fiber surface. During phagocytosis by alveolar macrophages, fibers are retained within phagolysosomes, and iron residues anchored at specific sites can catalyse radical formation. It has been demonstrated that intracellular Fe^{2+} overload promotes lipid peroxide accumulation, leading to DNA damage and ferroptosis, an iron-dependent form of programmed cell death. In line with this, both FER5 and MOL1 induced significant cytotoxic effects in MRC5 cells after 48 h, comparable to AMS1. Taken together, these results indicate that ferrierite and mordenite, although not currently classified as carcinogenic, can elicit cytotoxic responses comparable to those of erionite. This finding suggests that certain fibrous zeolites presently regarded as low-risk materials may, under prolonged exposure, pose underestimated health hazards and warrant further toxicological assessment. Conversely, SC1 fibers did not affect cell viability, likely due to their structure, which allows efficient intracellular digestion without impairing cellular viability. This observation further supports the idea that lysosomal acidification is not a necessary factor for cytotoxicity. Overall, these results indicate that the investigated fibers induce qualitatively different modes of membrane perturbation.

Our findings are intriguing and consistent with previous studies investigating zeolite cytotoxicity in various in vitro models. Specifically, erionite fibers have been shown to induce necrotic cell death, leading to the release of damage-associated high-mobility group protein 1 (HMGB-1) into the extracellular space (Ballirano et al., 2025). Furthermore, erionite has also been reported to disrupt intracellular calcium homeostasis and trigger apoptosis (Ballirano et al., 2025; Gualtieri, 2023). A recent in vitro toxicity study on human lung cells demonstrated that erionite induces apoptosis, oxidative stress and DNA damage in a dose-dependent manner. Moreover, both acute (24–72 h) and early-chronic (7 d) responses included increased expression of multiple cytokines, along with fibrotic and Epithelial to Mesenchymal transition (EMT) markers (Scarfì et al., 2025).

Interestingly, our Trypan Blue and Calcein-AM assays revealed a marked reduction in cell viability - approximately 50% - in MRC-5 cells exposed to MOL1, comparable to the response observed for erionite (AMS1). Although mordenite is generally considered non-mutagenic, its cytotoxic potential increases in the presence of ferrous ions, as shown in the AS52 ovary cell line. Fach et al. (2003) also reported that mordenite induces an oxidative burst in a pulmonary alveolar macrophage-derived cell line, producing high levels of hydroxyl radicals similar to erionite,

Table 3
Integrated toxicity potential of the investigated zeolite fibers based on morphology, specific surface area (SSA), chemical stability (Si/Al ratio), and observed biological responses.

Zeolite fiber	Fiber morphology	Specific surface area (SSA)	Si/Al ratio	Key biological responses	Integrated toxicity potential
Erionite (AMS1)	Very small fibers; strong fragmentation	High	Moderate	Strong membrane interaction, high ROS production, reduced cell viability	Very high
Ferrierite (FER5)	Small fibers; moderate fragmentation	Intermediate	High	Elevated ROS production; cytotoxic effects after prolonged exposure	High
Mordenite (MOL1)	Limited fibrous development	Intermediate–high	High	Significant cytotoxicity (~50% viability reduction); oxidative stress	Moderate–High
Scolecite (SC1)	Minimal fibrous character	Very low	Low	Weak membrane interaction; negligible cytotoxicity	Low

an effect attributed to iron associated with the fiber surface. The combination of morphological, EPR, and cytotoxicity data underscores how fiber structure, surface chemistry, and persistence within the cellular environment collectively determine biological outcomes. This integrated evidence supports the hypothesis that fiber-induced oxidative stress and lysosomal impairment constitute early events that drive chronic inflammation and, potentially, neoplastic transformation. Overall, these findings support the role of zeolite fibers as contributors to inflammation and suggest their potential involvement in the development of chronic diseases and malignancies over time. Although this study has some limitations, a more comprehensive understanding of the lung's response to fibrous zeolites will require investigating the interactions between MRC-5 cells, alveolar epithelial cells, and other relevant cell types to better elucidate the underlying signaling pathways and mechanisms of action. Moreover, long-term studies that mimic chronic fiber exposure are critical for identifying the inflammatory pathways and molecular mechanisms responsible for fiber-induced pathogenicity. This study therefore provides an important foundation for elucidating the biological mechanisms underlying the toxicity and carcinogenic potential of fibrous zeolites, while enhancing our understanding of the associated health risks.

5. Conclusions

Our planet hosts numerous fibrous mineral species, many of which occur in stone materials used for industrial and commercial purposes or are naturally present in rocks and soils that can be disturbed or mobilized by human activity. Because the interactions between many of these minerals and biological systems remain poorly understood, investigating and characterizing their toxicity is essential.

The present results highlight a clear relationship between the physicochemical properties of fibrous zeolites and their biological effects (Table 3). Fiber morphology appears to play a primary role, as minerals characterized by smaller diameters and a greater tendency to fragment, such as erionite (AMS1) and ferrierite (FER5), generate a larger proportion of inhalable particles capable of interacting with cellular membranes. These morphological features, together with higher specific surface areas, enhance fiber reactivity and increase the likelihood of membrane perturbation and cellular uptake. Chemical composition also contributes to toxicity through its influence on biopersistence: the relatively high Si/Al ratios of ferrierite and mordenite suggest greater stability under physiological conditions, potentially favoring prolonged residence in lung tissues. In addition, even trace amounts of transition metals, particularly Fe, may amplify biological responses by promoting reactive oxygen species (ROS) formation. Consistent with this interpretation, EPR measurements revealed stronger and more persistent membrane interactions for erionite compared with ferrierite and scolecite, correlating with reduced cell viability and increased oxidative stress. The elevated intracellular ROS levels and lysosomal alterations observed in MRC-5 fibroblasts further support the role of oxidative stress and impaired intracellular processing as key early events in fiber-induced cytotoxicity. Overall, these findings indicate that the combined effects of fiber morphology, surface reactivity, chemical stability, and trace element content determine the biological impact of fibrous zeolites.

The results of this study demonstrate that zeolite fibers can markedly alter the cellular microenvironment of pulmonary fibroblasts, affecting both cell proliferation and function. Importantly, we report previously unrecognized biological effects of FER5, MOL1 and SC1 on human lung fibroblasts. In particular, our data show that FER5 and MOL1 exert cytotoxic effects comparable to those of erionite (AMS1), suggesting a potentially harmful impact on human health under conditions of prolonged exposure. These findings underscore the need to re-evaluate the toxic potential of fibrous zeolites beyond the traditionally recognized carcinogenic species. Future investigations integrating long-term exposure models and molecular pathway analyses will be essential to fully elucidate their pathogenic mechanisms. Such studies will be critical for anticipating the toxic potential of fibrous minerals, identifying their environmental or industrial occurrence, and ultimately supporting risk assessment efforts aimed at protecting public health.

CRediT authorship contribution statement

Matteo Giordani: Writing – review & editing, Supervision, Investigation, Formal analysis, Conceptualization. **Maria Gemma Nasoni:** Writing – review & editing, Investigation, Formal analysis, Data curation, Conceptualization. **Erik Bargagni:** Writing – review & editing, Formal analysis, Data curation. **Michela Cangiotti:** Writing – review & editing, Formal analysis, Data curation. **Francesca Luchetti:** Writing – review & editing, Formal analysis, Data curation. **Michele Mattioli:** Writing – review & editing, Project administration, Investigation, Funding acquisition, Formal analysis.

Declaration of competing interest

The authors declare the following financial interests/personal relationships which may be considered as potential competing interests: Michele Mattioli reports financial support and administrative support were provided by Italian Ministry of University and Research Prot. 20173X8WA4. If there are other authors, they declare that they have no known competing financial interests or personal relationships that could have appeared to influence the work reported in this paper.

Acknowledgments

This research was conducted under the project “Fibres: a multidisciplinary mineralogical, crystal-chemical and biological project to amend the paradigm of toxicity and carcinogenicity of mineral fibers” funded by the Italian Ministry of University and Research (PRIN: Progetti di Ricerca di Rilevante Interesse Nazionale - Bando 2017 - Prot. 20173X8WA4). The research was also funded by the 2022 research programs of the Department of Pure and Applied Sciences of the Università di Urbino Carlo Bo (project “New asbestiform fibers: mineralogical and physical-chemical characterization”, responsible M. Mattioli). We warmly thank PD Dr. Georgia Cametti for her support in acquiring SEM-EDX data of MOL1, and Laura Valentini for her

invaluable help during the ESEM observations. During the preparation of this work, the authors used AI-assisted writing tools to enhance language and readability.

Appendix A. Supplementary data

Supplementary data to this article can be found online at https://doi.org/10.1016/j.envpol.2026.128030.

Data availability

Data will be made available on request.

References

Adamis, Z., Tátrai, E., Honma, K., Six, É., Ungváry, G., 2000. In vitro and in vivo tests for determination of the pathogenicity of quartz, diatomaceous Earth, mordenite and clinoptilolite. Ann. Occup. Hyg. 44, 67–74.

Aguilar-Armenta, G., Patiño-Iglesias, M.E., 2002. Adsorption equilibria and kinetics of propylene and propane on natural erionite and on erionite exchanged with K^+ and Ag^+. Langmuir 18, 7456–7461.

Altenbach, C., 1995. Monte Carlo simulation program for EPR spectra analysis. University of California, Los Angeles (unpublished software).

Armbruster, T., Gunter, M.E., 2001. Crystal structures of natural zeolites. In: Bish, D.L., Ming, D.W. (Eds.), Natural Zeolites: Occurrence, Properties, Applications, Reviews in Mineralogy and Geochemistry, vol. 45. Mineralogical Society of America, Washington, DC, USA, pp. 1–67. https://doi.org/10.2138/rmg.2001.45.1.

Aust, A.E., Cook, P.M., Dodson, R.D., 2001. Morphological and chemical mechanisms of elongated mineral particle toxicities. J. Toxicol. Environ. Health B 14, 40–75. https://doi.org/10.1080/10937404.2011.556046.

Ballirano, P., Pacella, A., Bloise, A., Giordani, M., Mattioli, M., 2018. Thermal stability of woolly erionite-K and considerations about the heat-induced behaviour of the erionite group. Minerals 8 (1), 28. https://doi.org/10.3390/min8010028.

Ballirano, P., Pacella, A., Cremisini, C., Nardi, E., Fantauzzi, M., Atzei, D., Rossi, A., Cametti, G., 2015. Fe (II) segregation at a specific crystallographic site of fibrous erionite: a first step toward the understanding of the mechanisms inducing its carcinogenicity. Microporous Mesoporous Mater. 211, 49–63.

Ballirano, P., Pacella, A., Mirata, S., Passalacqua, M., Di Carlo, M.C., Arrizza, L., Montereali, M.R., Scarfì, S., 2025. Fibrous erionite modifications following THP-1 macrophage phagocytosis: an insight into the mechanisms of interaction with biological systems. J. Hazard. Mater., 137546 https://doi.org/10.1016/j.jhazmat.2025.137546.

Beaucham, C., King, B., Feldmann, K., Harper, M., Dozier, A., 2018. Assessing occupational erionite and respirable crystalline silica exposure among outdoor workers in Wyoming, South Dakota, and Montana. J. Occup. Environ. Hyg. 15 (6), 455–465. https://doi.org/10.1080/15459624.2018.1447116.

Betti, M., Nasoni, M.G., Luchetti, F., Giordani, M., Mattioli, M., 2022. Potential toxicity of natural fibrous zeolites: in vitro study using Jurkat and HT22 cell lines. Minerals 12 (8), 988. https://doi.org/10.3390/min12080988.

Bloise, A., Barca, D., Gualtieri, A.F., Pollastri, S., Belluso, E., 2016. Trace elements in hazardous mineral fibres. Environ. Pollut. 216, 314–323. https://doi.org/10.1016/j.envpol.2016.06.007.

Bloise, A., Ricchiuti, C., Punturo, R., Pereira, D., 2020. Potentially toxic elements (PTEs) associated with asbestos chrysotile, tremolite and actinolite in the Calabria region (Italy). Chem. Geol. 558, 119896. https://doi.org/10.1016/j.chemgeo.2020.119896.

Boulanger, G., Andujar, P., Pairon, J.C., Billon-Galland, M.A., Dion, C., Dumortier, P., Brochard, P., Sobaszek, A., Bartsch, P., Paris, C., Jaurand, M.C., 2014. Quantification of short and long asbestos fibers to assess asbestos exposure: a review of fiber size toxicity. Environ. Health 13, 59. https://doi.org/10.1186/1476-069X-13-59.

Cametti, G., Pacella, A., Mura, F., Rossi, M., Ballirano, P., 2013. New morphological, chemical, and structural data of woolly erionite-Na from Durkee, Oregon, USA. Am. Mineral. 98, 2155–2163. https://doi.org/10.2138/am.2013.4474.

Cangiotti, M., Battistelli, M., Salucci, S., Falcieri, E., Mattioli, M., Giordani, M., Ottaviani, M.F., 2017. Electron paramagnetic resonance and transmission electron microscopy study of the interactions between asbestiform zeolite fibers and model membranes. J. Toxicol. Environ. Health, Part A 80 (3), 171–187. https://doi.org/10.1080/15287394.2016.1275901.

Cangiotti, M., Salucci, S., Battistelli, M., Falcieri, E., Mattioli, M., Giordani, M., Ottaviani, M.F., 2018. EPR, TEM and cell viability study of asbestiform zeolite fibers in cell media. Colloids Surf. B Biointerfaces 161, 147–155. https://doi.org/10.1016/j.colsurfb.2017.10.045.

Carbone, M., Baris, Y.I., Bertino, P., Brass, B., Comertpay, S., Dogan, A.U., Gaudino, G., Jube, S., Kanodia, S., Partridge, C.R., Pass, H.I., 2011. Erionite exposure in North Dakota and Turkish villages with mesothelioma. Proc. Natl. Acad. Sci. USA 108 (33), 13618–13623.

Chen, X., Guo, C., Kong, J., 2012. Oxidative stress in neurodegenerative diseases. Neural Regen. Res. 7 (5), 376–385. https://doi.org/10.3969/j.issn.1673-5374.2012.05.009.

Corma, A., Miguel, P.J., Orchilles, A.V., Koermer, G., 1994. Zeolite effects on the cracking of long chain alkyl aromatics. J. Catal. 145, 181–186. https://doi.org/10.1006/jcat.1994.1021.

Di Giuseppe, D., 2020. Characterization of fibrous mordenite: a first step for the evaluation of its potential toxicity. Crystals 10 (9), 769. https://doi.org/10.3390/cryst10090769.

Dogan, A.U., Dogan, M., 2008. Re-evaluation and re-classification of erionite series minerals. Environ. Geochem. Health 30, 355–366.

Eakle, A.S., 1898. Erionite, a new zeolite. Am. J. Sci. 4 (31), 66–68.

Eroglu, N., Emekci, M., Athanassiou, C.G., 2017. Applications of natural zeolites on agriculture and food production. J. Sci. Food Agric. 97, 3487–3499. https://doi.org/10.1002/jsfa.8312.

Fach, E., Kristovich, R., Long, J.F., Waldman, W.J., Dutta, P.K., Williams, M.V., 2003. The effect of iron on the biological activities of erionite and mordenite. Environ. Int. 29, 451–458.

Giordani, M., Ballirano, P., Pacella, A., Meli, M.A., Roselli, C., Di Lorenzo, F., Fagiolino, I., Mattioli, M., 2022a. Another potentially hazardous zeolite from northern Italy: fibrous mordenite. Minerals 12 (5), 627. https://doi.org/10.3390/min12050627.

Giordani, M., Cametti, G., Di Lorenzo, F., Churakov, S.V., 2019. Real-time observation of fibrous zeolites reactivity in contact with simulated lung fluids (SLFs) obtained by atomic force microscope (AFM). Minerals 9 (2), 83. https://doi.org/10.3390/min9020083.

Giordani, M., Mattioli, M., Ballirano, P., Pacella, A., Cenni, M., Boscardin, M., Valentini, L., 2017. Geological occurrence, mineralogical characterization, and risk assessment of potentially carcinogenic erionite in Italy. J. Toxicol. Environ. Health B 20 (2), 81–103. https://doi.org/10.1080/10937404.2016.1263586.

Giordani, M., Mattioli, M., Cangiotti, M., Fattori, A., Ottaviani, M.F., Betti, M., Ballirano, P., Pacella, A., Di Giuseppe, D., Scognamiglio, V., Hanuskova, M., 2022b. Characterisation of potentially toxic natural fibrous zeolites by means of electron paramagnetic resonance spectroscopy and morphological-mineralogical studies. Chemosphere 291, 133067. https://doi.org/10.1016/j.chemosphere.2021.133067.

Giordani, M., Meli, M.A., Roselli, C., Betti, M., Peruzzi, F., Taussi, M., Valentini, L., Fagiolino, I., Mattioli, M., 2022c. Could soluble minerals be hazardous to human health? Evidence from fibrous epsomite. Environ. Res. 206. https://doi.org/10.1016/j.envres.2021.112579.

Giordani, M., Mirata, S., Scarfi, S., Passalacqua, M., Fornasini, L., Drava, G., Meli, M.A., Roselli, C., Mattioli, M., 2025. The cytotoxic/genotoxic role of impurities in soluble minerals: the case of natural (fibrous epsomite) versus synthetic (Epsom salt) magnesium sulphate. Sci. Total Environ. 966, 178666. https://doi.org/10.1016/j.scitotenv.2025.178666.

Goldstein, J.I., Newbury, D.E., Echlin, P., Joy, D.C., Romig, A.D., Lyman, C.E., Fiori, C., Lifshin, E., 1992. Scanning Electron Microscopy and X-Ray Microanalysis, second ed. Plenum Press, New York, N.Y.

Gualtieri, A.F., 2023. Journey to the centre of the lung. The perspective of a mineralogist on the carcinogenic effects of mineral fibres in the lungs. J. Hazard. Mater. 442, 130077.

Gualtieri, A.F., Gandolfi, N.B., Passaglia, E., Pollastri, S., Mattioli, M., Giordani, M., Ottaviani, M.F., Cangiotti, M., Bloise, A., Barca, D., Vigliaturo, R., 2018a. Is fibrous ferrierite a potential health hazard? Characterization and comparison with fibrous erionite. Am. Mineral. 103 (7), 1044–1055. https://doi.org/10.2138/am-2018-6508.

Gualtieri, A.F., Pollastri, S., Bursi Gandolfi, N., Gualtieri, M.L., 2018b. In vitro acellular dissolution of mineral fibres: a comparative study. Sci. Rep. 8 (1), 7071. https://doi.org/10.1038/s41598-018-25531-4.

Guthrie, G.D., 1992. Biological effects of inhaled minerals. Am. Mineral. 77, 225–243.

Hartman, R.L., Fogler, H.S., 2007. Understanding the dissolution of zeolites. Langmuir 23, 5477–5484.

Hernández, M.A., Corona, L., Rojas, F., 2000. Adsorption characteristics of natural erionite, clinoptilolite and mordenite zeolites from Mexico. Adsorption 6, 33–45.

Heyder, J., Gebhart, J., Rudolf, G., Schiller, C.F., Stahlhofen, W., et al., 1986. Deposition of particles in the human respiratory tract in the size range 0.005-15 μm. J. Aerosol Sci. 5, 811–825.

IARC (International Agency for Research on Cancer), 1997. Silica, some silicates, coal dust and para-aramid fibrils. In: IARC Monographs on the Evaluation Carcinogenic Risks to Humans, vol. 42. IARC Publication, Lyon, France, pp. 225–239.

IARC (International Agency for Research on Cancer), 2012. Monographs Vol. 100C Evaluation of Carcinogenic Risks to Humans. International Agency for Research on Cancer, Lyon, France.

Ilgren, E.B., Kazemain, H., Hoskins, J.A., 2015. Kandovan the next 'Capadoccia'? – a potential public health issue for erionite related mesothelioma risk. Epidemiol. Biostat. Publ. Health 12 (1).

Korchevskiy, A.A., Wylie, A.G., 2021. Dimensional determinants for the carcinogenic potency of elongate amphibole particles. Inhal. Toxicol. 33 (6-8), 244–259.

Korkuna, O., Leboda, R., Skubiszewska-Zie, B.J., Vrublevs'Ka, T., Gun'Ko, V.M., Ryczkowski, J., 2006. Structural and physicochemical properties of natural zeolites: clinoptilolite and mordenite. Microporous Mesoporous Mater. 87 (3), 243–254.

Lee, K.P., 1985. Lung response to particulates with emphasis on asbestos and other fibrous dust. Crit. Rev. Toxicol. 14, 33–86. https://doi.org/10.3109/10408448509023764.

Lycourghiotis, S., Makarouni, D., Kordouli, E., Bourikas, K., Kordulis, C., Dourtoglou, V., 2018. Activation of natural mordenite by various acids: characterization and evaluation in the transformation of limonene into p-cymene. Mol. Catal. 450, 95–103.

Mattioli, M., Ballirano, P., Pacella, A., Cangiotti, M., Di Lorenzo, F., Valentini, L., Meli, M.A., Roselli, C., Fagiolino, I., Giordani, M., 2022. Fibrous ferrierite from northern Italy: mineralogical characterization, surface properties, and assessment of potential toxicity. Minerals 12 (5), 626. https://doi.org/10.3390/min12050626.

Mattioli, M., Giordani, M., Arcangeli, P., Valentini, L., Boscardin, M., Pacella, A., Ballirano, P., 2018. Prismatic to asbestiform offretite from Northern Italy: occurrence, morphology and crystal-chemistry of a new potentially hazardous zeolite. Minerals 8 (2), 69. https://doi.org/10.3390/min8020069.

Mattioli, M., Giordani, M., Dogan, M., Cangiotti, M., Avella, G., Giorgi, R., Dogan, A.U., Ottaviani, M.F., 2016. Morpho-chemical characterization and surface properties of carcinogenic zeolite fibers. J. Hazard Mater. 306, 140–148. https://doi.org/10.1016/j.jhazmat.2015.11.015.

Mertens, G., Snellings, R., Van Balen, K., Bicer-Simsir, B., Verlooy, P., Elsen, J., 2009. Pozzolanic reactions of common natural zeolites with lime and parameters affecting their reactivity. Cement Concr. Res. 39 (3), 233–240. https://doi.org/10.1016/j.cemconres.2008.11.008.

Ming, D.W., Allen, E.R., 2001. Use of natural zeolites in agronomy, horticulture and environmental soil remediation. In: Bish, D.L., Ming, D.W. (Eds.), Natural Zeolites: Occurrence, Properties, Applications, Reviews in Mineralogy and Geochemistry, vol. 45. Mineralogical Society of America, Washington, DC, USA, pp. 619–654. https://doi.org/10.2138/rmg.2001.45.1.

Mirata, S., Almonti, V., Di Giuseppe, D., Fornasini, L., Raneri, S., Vernazza, S., Bersani, D., Gualtieri, A.F., Bassi, A.M., Scarfì, S., 2022. The acute toxicity of mineral fibres: a systematic in vitro study using different THP-1 macrophage phenotypes. Int. J. Mol. Sci. 23 (5), 2840. https://doi.org/10.3390/ijms23052840.

Narayanan, S., Tamizhdurai, P., Mangesh, V.L., Ragupathi, C., Ramesh, A., 2021. Recent advances in the synthesis and applications of mordenite zeolite–review. RSC Adv. 11 (1), 250–267.

National Institute for Occupational Safety and Health (NIOSH), 1994a. NIOSH method 7400. Asbestos and other fibers by PCM. In: NIOSH Manual of Analytical Methods, fourth ed.

National Institute for Occupational Safety and Health (NIOSH), 1994b. NIOSH method 7402. Asbestos by TEM. In: NIOSH Manual of Analytical Methods, fourth ed.

Niwa, M., Katada, N., Okumura, K., 2010. Characterization and Design of Zeolite Catalysts: Solid Acidity, Shape Selectivity and Loading Properties, vol. 141. Springer Science & Business Media.

Ortega-Guerrero, M.A., Carrasco-Núñez, G., 2014. Environmental occurrence, origin, physical and geochemical properties, and carcinogenic potential of erionite near San Miguel de Allende, Mexico. Environ. Geochem. Health 36, 517–529.

Pacella, A., Ballirano, P., Cametti, G., 2016. Quantitative chemical analysis of erionite fibres using a micro-analytical SEM-EDX method. Eur. J. Mineral 28, 257–264.

Pacella, A., Ballirano, P., Fantauzzi, M., Rossi, A., Nardi, E., Capitani, G., Arrizza, L., Montereali, M.R., 2021. Surface and bulk modifications of amphibole asbestos in mimicked gamble's solution at acidic pH. Sci. Rep. 11 (1). https://doi.org/10.1038/s41598-021-93758-9. Articolo 1.

Pacella, A., Ballirano, P., Di Carlo, M.C., Fantauzzi, M., Rossi, A., Nardi, E., Viti, C., Arrizza, L., Campopiano, A., Cannizzaro, A., Bloise, A., Montereali, M.R., 2023. Dissolution reaction and surface modification of UICC amosite in mimicked gamble's solution: a step towards filling the gap between asbestos toxicity and its crystal chemical features. Nanomaterials 13 (22). https://doi.org/10.3390/nano13222933. Articolo 22.

Palekar, L.D., Most, B.M., Coffin, D.L., 1988. Significance of mass and number of fibers in the correlation of V79 cytotoxicity with tumorigenic potential of mineral fiber. Environ. Res. 46, 142–152.

Passaglia, E., 1970. The crystal chemistry of chabazites. Am. Mineral. 55 (7-8), 1278–1301.

Passaglia, E., Artioli, G., Gualtieri, A., 1998. Crystal chemistry of the zeolites erionite and offretite. Am. Mineral. 83 (5-6), 577–589.

Patel, J.P., Brook, M.S., 2021. Erionite asbestiform fibres and health risk in aotearoa/New Zealand: A research note. New Zealand Geograph. 77 (2), 123–129.

Pollastri, S., Gualtieri, A.F., Gualtieri, M.L., Hanuskova, M., Cavallo, A., Gaudino, G., 2014. The zeta potential of mineral fibres. J. Hazard. Mater. 276, 469–479.

Pugnaloni, A., Di Valerio, S.S., Tossetta, G., Armeni, T., Cianfruglia, L., Tiano, L., Marchegiani, F., Stipa, P., Laudadio, E., Sabbatini, S., Minnelli, C., Vaiasicca, S., Ramini, D., Procopio, A.D., Fazioli, F., Gualtieri, A.F., 2023. Cytotoxicity in vitro of two non-commercial samples of chrysotile and fibrous erionite. Per. Mineral. 92 (2), 241–259.

Saini-Eidukat, B., Triplett, J.W., 2014. Erionite and offretite from the killdeer Mountains, dunn county, North Dakota, USA. Am. Mineral. 99 (1), 8–15.

Salucci, S., Giordani, M., Betti, M., Valentini, L., Gobbi, P., Mattioli, M., 2024. The in vitro cytotoxic effects of natural (fibrous epsomite crystals) and synthetic (Epsom salt) magnesium sulfate. Microsc. Res. Tech. 87 (4), 685–694.

Sanchez, V.C., Pietruska, J.R., Miselis, N.R., Hurt, R.H., Kane, A.B., 2009. Biopersistence and potential adverse health impacts of fibrous nanomaterials: what have we learned from asbestos? Wiley Interdiscip. Rev., Nanomed. Nanobiotechnol. 1 (5), 511–529.

Scarfì, S., Almonti, V., Mirata, S., Passalacqua, M., Vernazza, S., Patel, J.P., Brook, M., Hamilton, A., Kah, M., Gualtieri, A.F., 2025. In vitro cyto-and geno-toxicity of asbestiform erionite from New Zealand. Environ. Res. 265, 120415.

Scharf, B., Clement, C.C., Zolla, V., Perino, G., Yan, B., Elci, S.G., Purdue, E., Goldring, S., Macaluso, F., Cobelli, N., Vachet, R.W., Santambrogio, L., 2014. Molecular analysis of chromium and cobalt-related toxicity. Sci. Rep. 4 (1), 5729. https://doi.org/10.1038/srep05729.

Stan, M.S., Badea, S., Hermenean, A., Herman, H., Trica, B., Sbarcea, B.G., Dinischiotu, A., 2021. New insights into the cell death signaling pathways triggered by long-term exposure to silicon-based quantum dots in human lung fibroblasts. Nanomaterials 11 (2), 323. https://doi.org/10.3390/nano11020323.

Stanton, M.F., Layard, M., Tegeris, A., Miller, E., May, M., Morgan, E., Smith, A., 1981. Relation of particles dimension to carcinogenicity in amphibole asbestosis and other fibrous minerals. J. Natl. Cancer Inst. 67, 965–975. https://doi.org/10.1093/jnci/67.5.965.

Stephenson, D.J., Fairchild, C.I., Buchan, R.M., Dakins, M.E., 1990. A fiber characterization of the natural zeolite, mordenite: a potential inhalation health hazard. Aerosol Sci. Technol. 30, 467–476.

Suzuki, Y., 1982. Carcinogenic and fibrogenic effects of zeolites: preliminary observations. Environ. Res. 27, 433–445.

Suzuki, Y., Kohyama, N., 1988. Carcinogenic and fibrogenic effects of erionite, mordenite, and synthetic zeolite 4A. In: Kallo, D., Sherry, H.S. (Eds.), Occurrence, Properties and Utilization of Natural Zeolites. Akadémiai Kiadò, Budapest, Hungary, pp. 829–840.

Suzuki, Y., Kohyama, N., 1984. Malignant mesothelioma induced by asbestos and zeolite in the mouse peritoneal cavity. Environ. Res. 35, 277–292.

Tátrai, E., Bácsy, E., Kárpáti, J., Ungváry, G., 1992. On the examination of the pulmonary toxicity of mordenite in rats. Pol. J. Occup. Med. Environ. Health 5, 237–243.

Timblin, C.R., Guthrie, G.D., Janssen, Y.W., Walsh, E.S., Vacek, P., Mossman, B.T., 1998. Patterns of c-fos and c-jun proto-oncogene expression, apoptosis, and proliferation in rat pleural mesothelial cells exposed to erionite or asbestos fibers. Toxicol. Appl. Pharmacol. 151 (1), 88–97. https://doi.org/10.1006/taap.1998.8450.

Vasylechko, V.O., Lebedynets, L.O., Gryshchouk, G.V., Leboda, R., Skubiszewska-Zięba, J., 1999. Investigations of usefulness of Transcarpathian zeolites in trace analysis of waters. Application of mordenite for the preconcentration of trace amounts of copper and cadmium. Chem. Anal. 44, 1013–1024.

Wahono, S.K., Stalin, J., Addai-Mensah, J., Skinner, W., Vinu, A., Vasilev, K., 2020. Physico-chemical modification of natural mordenite-clinoptilolite zeolites and their enhanced CO2 adsorption capacity. Microporous Mesoporous Mater. 294, 109871.

Wei, B., Yang, L., Zhu, O., Yu, J., Jia, X., Dong, T., Lu, R., 2014. Multivariate analysis of trace elements distribution in hair of pleural plaques patients and health group in a rural area from China. Hair Ther. Transplant. 4 (2). https://doi.org/10.4172/2167-0951.1000125.

World Health Organization (WHO), 1986. Asbestos and Other Natural Mineral Fibers, vol. 53. Environmental Health Criteria, Geneva, Switzerland, pp. 69–107.

Wylie, A.G., Korchevskiy, A., Segrave, A.M., Duane, A., 2020. Modeling mesothelioma risk factors from amphibole fiber dimensionality: mineralogical and epidemiological perspective. J. Appl. Toxicol. 40 (4), 515–524.

Zhou, L., Boyd, C.E., 2014. Total ammonia nitrogen removal from aqueous solutions by the natural zeolite, mordenite: a laboratory test and experimental study. Aquaculture 432, 252–257.

Zoboli, A., Di Giuseppe, D., Baraldi, C., Gamberini, M.C., Malferrari, D., Urso, G., Gualtieri, M.L., Bailey, M., Gualtieri, A.F., 2019. Characterisation of fibrous ferrierite in the rhyolitic tuffs at lovelock, Nevada, USA. Mineral. Mag. 83 (4), 577–586.